

AD_____

Award Number: W81XWH-09-2-0102

TITLE: Traumatic Brain Injury Diffusion Magnetic Resonance Imaging Research
Roadmap Development Project

PRINCIPAL INVESTIGATOR: Michael W. Vannier, M.D.

CONTRACTING ORGANIZATION: University of Chicago
Chicago, IL 60637-5418

REPORT DATE: October 2011

TYPE OF REPORT: Annual

PREPARED FOR: U.S. Army Medical Research and Materiel Command
Fort Detrick, Maryland 21702-5012

DISTRIBUTION STATEMENT: Approved for Public Release;
Distribution Unlimited

The views, opinions and/or findings contained in this report are those of the author(s) and should not be construed as an official Department of the Army position, policy or decision unless so designated by other documentation.

REPORT DOCUMENTATION PAGE				Form Approved OMB No. 0704-0188	
Public reporting burden for this collection of information is estimated to average 1 hour per response, including the time for reviewing instructions, searching existing data sources, gathering and maintaining the data needed, and completing and reviewing this collection of information. Send comments regarding this burden estimate or any other aspect of this collection of information, including suggestions for reducing this burden to Department of Defense, Washington Headquarters Services, Directorate for Information Operations and Reports (0704-0188), 1215 Jefferson Davis Highway, Suite 1204, Arlington, VA 22202-4302. Respondents should be aware that notwithstanding any other provision of law, no person shall be subject to any penalty for failing to comply with a collection of information if it does not display a currently valid OMB control number. PLEASE DO NOT RETURN YOUR FORM TO THE ABOVE ADDRESS.					
1. REPORT DATE October 2011		2. REPORT TYPE Annual		3. DATES COVERED 14 September 2010 – 13 September 2011	
4. TITLE AND SUBTITLE Traumatic Brain Injury Diffusion Magnetic Resonance Imaging Research Roadmap Development Project				5a. CONTRACT NUMBER	
				5b. GRANT NUMBER W81XWH-09-2-0102	
				5c. PROGRAM ELEMENT NUMBER	
6. AUTHOR(S) Michael W. Vannier, M.D. E-Mail: mvannier@radiology.bsd.uchicago.edu				5d. PROJECT NUMBER	
				5e. TASK NUMBER	
				5f. WORK UNIT NUMBER	
7. PERFORMING ORGANIZATION NAME(S) AND ADDRESS(ES) University of Chicago Chicago, IL 60637-5418				8. PERFORMING ORGANIZATION REPORT NUMBER	
9. SPONSORING / MONITORING AGENCY NAME(S) AND ADDRESS(ES) U.S. Army Medical Research and Materiel Command Fort Detrick, Maryland 21702-5012				10. SPONSOR/MONITOR'S ACRONYM(S)	
				11. SPONSOR/MONITOR'S REPORT NUMBER(S)	
12. DISTRIBUTION / AVAILABILITY STATEMENT Approved for Public Release; Distribution Unlimited					
13. SUPPLEMENTARY NOTES					
14. ABSTRACT Traumatic Brain Injury (TBI) is a public health problem of immense magnitude and immediate importance that has become endemic among military personnel and veterans. Imaging biomarkers of TBI are needed to support diagnosis and therapy and to predict TBI consequences while avoiding further injury. Diffusion magnetic resonance imaging has potential to become the non-invasive tool of choice for TBI structural assessment. Despite its potential, realizing the benefits of diffusion MRI in TBI requires a base of evidence for decision making that requires multi-organizational coordination and planning. The purpose of this proposed research is to synthesize a roadmap for diffusion MR imaging in brain traumatic injury that can advance the field and deliver the benefits most effectively in the shortest period of time. Essential steps toward implementation of the plan will be taken thereafter.					
15. SUBJECT TERMS None provided.					
16. SECURITY CLASSIFICATION OF:			17. LIMITATION OF ABSTRACT	18. NUMBER OF PAGES	19a. NAME OF RESPONSIBLE PERSON
a. REPORT	b. ABSTRACT	c. THIS PAGE			USAMRMC
U	U	U	UU	ii	19b. TELEPHONE NUMBER (include area code)

INTRODUCTION

Traumatic Brain Injury (TBI) is a public health problem of immense magnitude and immediate importance that has become endemic among military personnel and veterans.

Imaging biomarkers of TBI are needed to support diagnosis and therapy and to predict TBI consequences while avoiding further injury. Diffusion magnetic resonance imaging has potential to become the non-invasive tool of choice for TBI structural assessment. Despite its potential, realizing the benefits of diffusion MRI in TBI requires a base of evidence for decision making that can only be assembled by multi-organizational coordination and planning.

The purpose of this research is to synthesize a roadmap for diffusion MR imaging in brain traumatic injury that can advance the field and deliver the benefits most effectively in the shortest period of time. Essential steps toward implementation of the plan will be taken to accelerate translation of the technology into clinical practice.

A roadmapping meeting was organized and conducted in June 2010 to assess state-of-the-art practice in brain traumatic injury imaging research and to propose specific recommendations regarding: (1) the standardization of diffusion imaging techniques, (2) the validation of the accuracy and clinical utility of imaging markers of the white matter injury, (3) the validation of imaging biomarkers relevant to clinical outcomes, and (4) the creation of a central repository to achieve these goals. This project implements a process to create these recommendations and examine practical steps to achieve them.

At present, an established medical method for quantitative, sensitive and specific evaluation of closed head traumatic brain injury does not exist. Many technologies are being utilized such as blood work, X-ray, computed tomography scan (CT), magnetic resonance imaging (MRI), and electroencephalogram (EEG), but perhaps the most promising technology on the horizon is the Diffusion Tensor Imaging (DTI). Diffusion tensor imaging (DTI) is a magnetic resonance imaging (MRI)-based technique that allows the visualization, location, and orientation, of the brain's white matter tracts to determine changes in the brain due to blast, contact and related traumatic brain injuries. There is a critical and immediate need to use these tools to measure and track long term changes in the brain. The potential for DTI to improve our understanding of TBI has not been fully explored and challenges associated with non-existent standard practices amongst researchers and manufacturers remain a major challenge that this award will attempt to address through the design of a roadmap. Ultimately, imaging biomarkers for TBI may be identified, qualified and validated as a result of the roadmap.

On completion, this project will provide a 5-year roadmap for diffusion MR imaging for TBI achieved using a consensus process, with specific recommendations for imaging protocols, post-processing tools, quality control standards, and a shared image repository. The recommendations will be disseminated and pilot tested. A DTI of TBI post-processing workshop will be conducted. A testbed archive, informatics grid infrastructure, and post-processing software toolsets will be supported by practical implementations to guide further development and disseminate the technology.

BODY:

There is need to develop D-MRI into a qualified and validated biomarker by adapting methods and using best practices for other neuroimaging biomarkers. We are engaged in identifying the barriers to progress, especially for multidisciplinary (MRI physics, computer science/image processing, and especially TBI clinical practice) collaboration. There is greater recognition now of the need for a persistent information infrastructure to manage D-MRI and related clinical data in TBI patients as a means of fostering independent or secondary analyses and to encourage collaborations among disparate centers who collect this data.

TBI Database

According to NIH, more than 1.7 million Americans sustain a TBI each year, mostly from common causes. This includes the more than 200,000 service members who have been diagnosed with TBI over the last 12 years — most of those injuries being combat-related. No two brain injuries look or act exactly alike. The damage to the brain and its location is unique, as are the mix of symptoms that go with it. For example, research has shown that blast-related TBI, such as that suffered in combat, can present very differently than other types of TBI. (1)

With this variability in mind, DoD and NIH are partnering on the creation of a central TBI database. The hope is that by collecting uniform data on as many types of these injuries as possible, the database will be useful for research into the injury and help accelerate comparative effectiveness research on brain injury treatment and diagnosis.

The Federal Interagency Traumatic Brain Injury (FITBIR) database was announced in September 2011, and will be funded over the next four years. (1) NIH's Center for Information Technology will build it, based on experience when building the National Database on Autism Research.

The National Institute of Neurological Disorders and Stroke and the U.S. Army Medical Research and Materiel Command will partner in providing program support for the project and help fill the database with useful information. Researchers will be provided with exactly what kind of information FITBIR is looking for and will be encouraged to participate at the time they submit proposals for new TBI studies. (1)

The US National Institute of Health (NIH) Center for Information Technology (CIT) has developed the National Database for Autism Research (NDAR) (<http://ndar.nih.gov/>) a portal into multiple databases of autism spectrum disorders (ASD) related information. NDAR provides qualified researchers a place to submit their data, and allows scientists access to this data in order to perform studies. The result is a growing site of indexed information that can track a patient's results from different studies at different times. NDAR is a tool for ASD research. As it develops, it could provide insight into the disorder, and lead us to better understand its causes and its treatments.

NDAR is a data repository and portal to many other research repositories. Using NDAR, a researcher can query data from multiple repositories at the same time. This allows for re-aggregation, re-use, re-analysis, and rigorous comparison of results. Currently, NDAR shares

detailed clinical, genomic, imaging and other rich data from 17,000 research subjects. Data from another 45,000 subjects is expected. Compared to only 8% of data which is typically shared by any other major research communities, NDAR is poised to meet the Interagency Autism Strategic Plan goal of making 90% of all autism research data available. Fostering transparency, the NDAR website provides summary information about funded research to scientists and the general public. Pooling data across labs transforms research from a traditional, single-lab, single-project approach to a collaborative approach with unprecedented potential for discoveries. (2)

What makes NDAR so promising is the scope of its data. The NDAR Central Repository was formed from the NIH's Autism Centers for Excellence. Along with that repository, the NDAR portal provides access to several other stores of important ASD information: The Autism Genetic Research Exchange has data on 1000+ families with ASD members. 30,000 individuals are tracked in the Interactive Autism Network. 3000 records on ASD patients are kept in the National Institute for Mental Health's Genetics Repository. NIMH's Transcriptional Atlas for Human Brain Disorders provides additional analysis and insight into ASD. The Pediatric MRI Data Repository has information on more than 500 normally developing children and youths. In total there are many tens of thousands of records covering genetic, phenotypic, imaging, clinical, and pedigree data relevant to ASD.

NDAR has instituted several standards for data exchange and submission. The most important is the Global Unique Identifier (GUID). The GUID correlates each patient with a unique identifier code. Not only does this protect the privacy of patients, it allows indexing between studies. If an individual (or family) was part of one study for the NIH, and another for the NIMH, now their information is grouped as belonging together. This maximizes the benefit scientists can gain from the NDAR portal by allowing researchers to compare these studies in direct and meaningful ways. GUID based studies (meta-studies of the research performed by others) aid in extracting meaningful information out of these separate databases. (3)

Unfortunately, NDAR is not quite ready for full access. While the Central Repository is available now, the partnered databases are slowly being rolled out. The Pediatric MRI Data Repository was linked in spring 2010, and the rest will follow on an unspecified schedule.

The possible importance of NDAR is high. Scientists will be able to freely add and review a huge cross referenced database of information pertinent to ASD. Instead of being limited to just a few hundred patients, they now have effective access to the data of tens of thousands. NDAR's data submission process will help keep that database full of only rigorously tested information and the Data Access Committee will ensure it is only available to those with legitimate research credentials.

DTI Post-Processing Software Tools Evaluation

Many groups worldwide have developed software tools for the pre-processing, visualization, and analysis of diffusion MRI datasets. Often these tools are developed for a single project at the authors' institution, and then offered in the public domain for general applications. In

many instances, there are open source public domain tools that offer functionality that is superior to any available commercial product.

In this project, we hypothesize that one of the most important hindrances to the development of tools for traumatic brain injury evaluation using diffusion MRI is that sample datasets are unavailable. To remedy this situation, we plan to organize a workshop at a major international meeting where tool developers will be provided with TBI datasets obtained using MRI. The participants will have time in advance of the meeting to adapt their tools to the specific needs of TBI image analysis and can present their results in an open forum. Similar workshops using this approach were very successful in the processing of gene expression microarray datasets, so we intend to use their framework to advance TBI image analysis.

In preparation, we identified many common public domain software tools that were suitable for handling DTI datasets. Some of these tools are remarkably powerful and well developed. They may have thousands of users worldwide already, principally working on neuroimaging unrelated to trauma. Our intent has been to incorporate a representative sampling of different tools into our working environment, and test them ourselves using normal control and DTI traumatic brain injury datasets.

Numerous tools were identified and the software was downloaded and installed on our laboratory computer, a Dell Alienware Area 51 ALX desktop computer (12 Gbytes RAM, 4Tbytes of RAID disk storage). The tools installed were tabulated in the following list. These software tools were tested for data browsing, visualization and analysis and will see increasing use as the project goes forward. Some of these tools are Windows based and others are Linux based. To run Linux supported tools, a virtual machine player was installed on the computer which runs the Windows 7 Professional operating system. The table below lists relevant information on this collection of software tools.

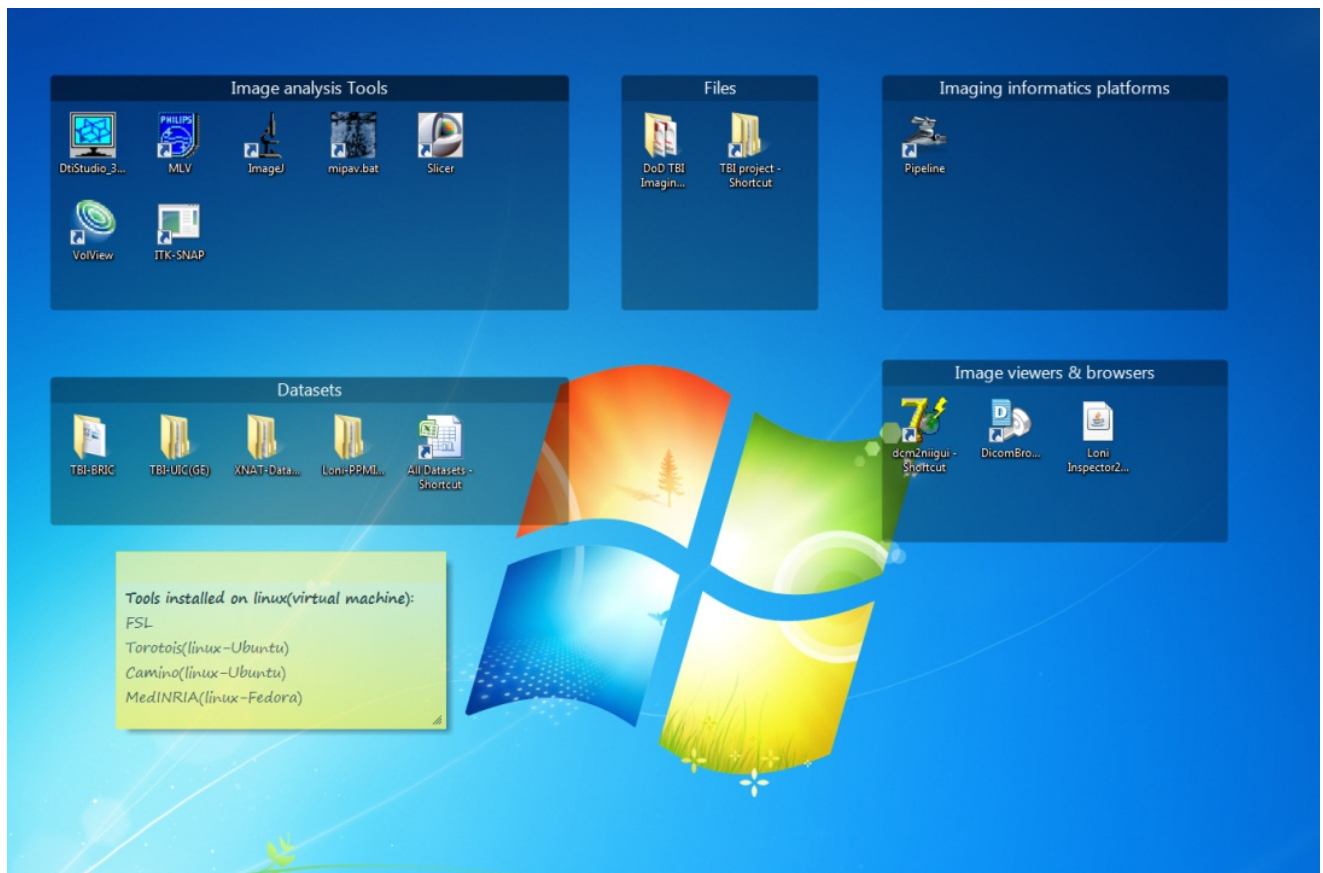
Software tools installed on the Area 51 ALX computer for DTI of TBI image analysis

Name	Type	Developer/Sponsors	Purposes and Features
FSL	Tool	Analysis Group, FMRI, Oxford, UK	Image Visualization and processing
DTI studio	Tool	Laboratory of Brain Anatomical MRI and Center for Imaging Science at Johns Hopkins University.	Image Viewer/ Diffusion Tensor Calculations/ Fiber Tracking and Editing/ 3D Visualization/ Image File Management/ Region of Interesting (ROI) Drawing and Statistics/ Image Registration
Tortoise	Tool	National Institute of Child Health and Human Development (NICHD)	Image resampling, motion, eddy current distortion and susceptibility induced EPI distortion corrections, and for re-orientation of data to a common space/software for tensor fitting, error analysis, color map visualization and ROI analysis

Slicer	Tool	Harvard University together with several contributors and Sponsors	Segmentation, registration and three-dimensional visualization of multi-modal image data, as well as advanced image analysis algorithms for diffusion tensor imaging, functional magnetic resonance imaging and image-guided therapy.
MedINRIA	Tool	INRIA Sophia Antipolis-France	Medical image processing and visualization: Diffusion Tensor Registration with Exact Finite Strain Differential/Log Euclidean Metrics/ HARDI: High angular resolution diffusion imaging/ Fiber Tracking/ Block Matching/ Diffeomorphic Demons
MIPAV	Tool	Center for Information Technology(CIT) -NIH	Medical Image Processing, Analysis, and Visualization with several features
Camino	Tool	University College London(UCL)	Analysis and reconstruction of Diffusion MRI data, tractography and connectivity mapping.
VolView	Tool	Kitware, Inc. -USA	Image visualization/Explore and analyze complex 3D medical or scientific data
itk-SNAP	Tool	University of Pennsylvania and University of Utah	segmentation of structures in 3D medical images
LONI Inspector	Tool	University of California,Los Angeles (UCLA)	Reading, displaying, searching, comparing, and exporting metadata from images
DICOM Browser	Tool	The Neuroinformatics Research Group - Washington University School of Medicine	Inspecting and modifying DICOM files
ImageJ	Tool	NIH	Image processing and analysis
Loni Pipeline	Tool	University of California,Los Angeles (UCLA)	A workflow application that allows users to describe their executable in a graphical user interface(module) and connect them together to create complex analyses
Loni	Platform	University of California,Los Angeles (UCLA)	Provides image database, software tools and computational algorithms and scientific approaches for the comprehensive and quantitative mapping of brain structure and function.
XNAT	Platform	Neuroinformatics Research Group at Washington University	Uploading, organizing and sharing data/View and Download data/ Search, explore and run complex processing on datasets
BIRN	Platform	NIH/NCCR	data-sharing infrastructure, software tools, strategies and advisory services

Testing the software tools was done as follows. A series of DTI datasets from different vendors (Philips, GE, and Siemens) were collected for use with the tools installed on the Area 51 ALX computer to test some of their functionality. The DTI datasets available to use originated from University of Chicago BRIC (Brain Research Imaging Center, Dr. Deborah Little's laboratory at UIC (University of Illinois), the PPMI (Parkinson's Progression Markers Initiative) database from LONI, and Washington University (St. Louis) XNAT database.

Below are screenshots of the computer desktop showing how these materials are organized, and screenshots of some excel datasheets related to the information of datasets collected in the computer.



Screenshot from the Area 51 ALX desktop computer, showing the organization of resources.

In the upper left are a collection of image analysis software tool icons. Each tool is activated by a mouse click. At the top center, file folders containing DoD TATRC TBI roadmap project images and documentation are shown. In the upper right the LONI pipeline icon is shown which provides access to remote resources at UCLA that can be applied as needed. In the bottom left are a collection of file folders containing sample DTI brain datasets, suitable for visualization and analysis. At the bottom right are image viewers and browsers that

handle the numerous data types encountered in this work, including DICOM, open and proprietary formats.

In the following illustration, the sample datasets are outlined. There are examples from UCMC BRIC, UIC, LONI (PPMI), and XNAT. Each entry in the first table points to a collection of individual datasets that are suitable for visualization and analysis function testing.

	Source	Number of datasets	Machine brand	Link
1	U of C-BRIC	4	Philips	Detailed list
2	UIC	8	GE	Detailed list
3	Loni(PPMI)	24	Siemens	Detailed list
4	XNAT	3	GE	Detailed list
Total		39		

PPMI Dataset info

Number	Image Data ID	Subject	Group	Sex	Age	Visit	Modality	Description	Type	Acq Date	Format	Link
1	243604	3154	PD	F	75	1	DTI	DTI_gated	Original	2/15/2011	DCM	DICOM Browser screenshot
2	243607	3154	PD	F	75	1	DTI	DTI_gated	Original	2/15/2011	DCM	DICOM Browser screenshot
3	243568	3151	Control	M	58	1	DTI	DTI_gated	Original	11/9/2010	DCM	DICOM Browser screenshot
4	243570	3151	Control	M	58	1	DTI	DTI_gated	Original	11/9/2010	DCM	DICOM Browser screenshot
5	243565	3112	Control	F	63	1	DTI	DTI_gated	Original	6/27/2011	DCM	DICOM Browser screenshot
6	243566	3112	Control	F	63	1	DTI	DTI_gated	Original	6/27/2011	DCM	DICOM Browser screenshot
7	243547	3111	PD	M	65	1	DTI	DTI_gated	Original	5/26/2011	DCM	DICOM Browser screenshot
8	243550	3111	PD	M	65	1	DTI	DTI_gated	Original	5/26/2011	DCM	DICOM Browser screenshot
9	232126	3109	Control	M	53	1	DTI	DTI_gated	Original	4/20/2011	DCM	DICOM Browser screenshot
10	232163	3108	PD	F	50	1	DTI	DTI_gated	Original	4/20/2011	DCM	DICOM Browser screenshot
11	232160	3108	PD	F	50	1	DTI	DTI_gated	Original	4/20/2011	DCM	DICOM Browser screenshot
12	232142	3107	PD	M	70	1	DTI	DTI_gated	Original	4/13/2011	DCM	DICOM Browser screenshot
13	232143	3107	PD	M	70	1	DTI	DTI_gated	Original	4/13/2011	DCM	DICOM Browser screenshot
14	232250	3106	Control	F	70	1	DTI	DTI_gated	Original	3/24/2011	DCM	DICOM Browser screenshot
15	232348	3106	Control	F	70	1	DTI	DTI_gated	Original	3/24/2011	DCM	DICOM Browser screenshot
16	226400	3105	PD	M	69	1	DTI	ep_b1000M46	Original	3/24/2011	DCM	DICOM Browser screenshot
17	226401	3105	PD	M	69	1	DTI	ep_b1000R30	Original	3/24/2011	DCM	DICOM Browser screenshot
18	226395	3104	Control	M	72	1	DTI	ep_b1000R2	Original	2/14/2011	DCM	DICOM Browser screenshot
19	226396	3104	Control	M	72	1	DTI	ep_b1000R9	Original	2/14/2011	DCM	DICOM Browser screenshot
20	226368	3102	PD	M	64	1	DTI	ep_b1000M48	Original	11/23/2010	DCM	DICOM Browser screenshot
21	226369	3102	PD	M	64	1	DTI	ep_b1000R19	Original	11/23/2010	DCM	DICOM Browser screenshot
22	248364	29124MAY11	Phantom	X	0	1	DTI	DTI	Original	5/24/2011	DCM	DICOM Browser screenshot
23	248363	08825MAR11	Phantom	M	75	1	DTI	DTI	Original	3/25/2011	DCM	DICOM Browser screenshot
24	248362	01216JUN11	Phantom	X	51	1	DTI	DTI	Original	6/16/2011	DCM	DICOM Browser screenshot

UofC(BRIC) Dataset info

Number	Study	Series	Acq Date	Format	Series Description	Link
1	343568399	701	11/22/2010	DCM	Survey	DICOM Browser screenshot
2		2201	11/22/2010	DCM	T1W_3D_TFE	DICOM Browser screenshot
3		2301	11/22/2010	DCM	DTI_3D	DICOM Browser screenshot
4		2401	11/22/2010	DCM	DTI_60	DICOM Browser screenshot
5		2501	11/22/2010	DCM	T1W_FFE	DICOM Browser screenshot
6		2601	11/22/2010	DCM	T1W_FFE	DICOM Browser screenshot
7	343674996	101	11/23/2010	DCM	(1) Survey	DICOM Browser screenshot
8		301	11/23/2010	DCM	DTI_3D	DICOM Browser screenshot
9		401	11/23/2010	DCM	(1) Survey	DICOM Browser screenshot
10		601	11/23/2010	DCM	DTI_3D	DICOM Browser screenshot
11		701	11/23/2010	DCM	DTI_60	DICOM Browser screenshot
12		702	11/23/2010	DCM	dWIP DTI_60 SENSE	DICOM Browser screenshot
13		703	11/23/2010	DCM	eWIP DTI_60 SENSE	DICOM Browser screenshot
14		704	11/23/2010	DCM	faWIP DTI_60 SENSE	DICOM Browser screenshot
15		705	11/23/2010	DCM	facWIP DTI_60 SENSE	DICOM Browser screenshot
16		801	11/23/2010	DCM	T1W_FFE	DICOM Browser screenshot
17		901	11/23/2010	DCM	T1W_FFE	DICOM Browser screenshot
18		1001	11/23/2010	DCM	WIP T1W_3D_TFE SENSE	DICOM Browser screenshot
19		1101	11/23/2010	DCM	WIP T1W_3D_TFE SENSE	DICOM Browser screenshot
20	344189037	0	11/29/2010	DCM		DICOM Browser screenshot
21		101	11/29/2010	DCM	(1) Survey	DICOM Browser screenshot
22		201	11/29/2010	DCM	(2) RefScan	DICOM Browser screenshot
23		301	11/29/2010	DCM	DTI_3D	DICOM Browser screenshot
24		302	11/29/2010	DCM	dWIP DTI_3D SENSE	DICOM Browser screenshot
25		303	11/29/2010	DCM	eWIP DTI_3D SENSE	DICOM Browser screenshot
26		304	11/29/2010	DCM	faWIP DTI_3D SENSE	DICOM Browser screenshot
27		305	11/29/2010	DCM	facWIP DTI_3D SENSE	DICOM Browser screenshot
28		401	11/29/2010	DCM	DTI_60	DICOM Browser screenshot
29		402	11/29/2010	DCM	dWIP DTI_60 SENSE	DICOM Browser screenshot
30		403	11/29/2010	DCM	eWIP DTI_60 SENSE	DICOM Browser screenshot
31		404	11/29/2010	DCM	faWIP DTI_60 SENSE	DICOM Browser screenshot
32		405	11/29/2010	DCM	facWIP DTI_60 SENSE	DICOM Browser screenshot
33		501	11/29/2010	DCM	T1W_FFE	DICOM Browser screenshot
34		601	11/29/2010	DCM	T1W_FFE	DICOM Browser screenshot
35		701	11/29/2010	DCM	WIP T1W_3D_TFE SENSE	DICOM Browser screenshot
36		801	11/29/2010	DCM	WIP T1W_3D_TFE SENSE	DICOM Browser screenshot
37		PR series0	11/29/2010	DCM		DICOM Browser screenshot
38		PR series0-0003	11/29/2010	DCM	(1) Survey	DICOM Browser screenshot
39		PR series0-0015	11/29/2010	DCM	DTI_3D	DICOM Browser screenshot
40		PR series0-0162	11/29/2010	DCM	faWIP DTI_3D SENSE	DICOM Browser screenshot
41		PR series0-0015	11/29/2010	DCM	T1W_FFE	DICOM Browser screenshot
42		PS series0-0158	11/29/2010	DCM	dWIP DTI_3D SENSE	DICOM Browser screenshot
43		PR series0-0160	11/29/2010	DCM	eWIP DTI_3D SENSE	DICOM Browser screenshot
44		PR series0-0166	11/29/2010	DCM	facWIP DTI_3D SENSE	DICOM Browser screenshot
45	344862599	101	12/7/2010	DCM	(1) Survey	DICOM Browser screenshot
46		301	12/7/2010	DCM	DTI_3D	DICOM Browser screenshot
47		302	12/7/2010	DCM	dWIP DTI_3D SENSE	DICOM Browser screenshot
48		303	12/7/2010	DCM	eWIP DTI_3D SENSE	DICOM Browser screenshot
49		304	12/7/2010	DCM	faWIP DTI_3D SENSE	DICOM Browser screenshot

Using the available tools, we intend to take D-MRI of TBI datasets from already published studies and attempt to reproduce the results with a much higher degree of automation that traditionally available. If successful, we can offer the ability to independently verify the results of various single-center clinical trials using D-MRI of TBI. This testing will provide experience to guide the organization of a workshop on post-processing of TBI datasets, as required by this project.

D-MRI of TBI Physics

Diffusion Tensor Imaging (DTI) is a promising MRI imaging technique that has significant potential to serve as a biomarker for diagnosis and assessment of patients with brain trauma. In the past one year, we have focused our efforts to develop DTI techniques dedicated to the efficient study of TBI patients. Data acquisition pulse sequence development was done with the expectation that they will be tested in conjunction with manufacturer-supplied sequences to evaluate test-retest reproducibility on a variety of platforms.

1. DTI phantom. We have selected and obtained a special designed DTI phantom that will be suitable for quality control on our TBI patient study. Initial testing shows that the DTI images acquired from this phantom have sufficient high sensitivity and high signal-to-noise that we needed for this project. We are in the process to further improve this phantom quality by removing air bubbles within the liquid. (4)

2. Standard DTI pulse sequences for TBI patients. Based on the recommendation made by a task force composed by a dozen MRI physicists who are expert in DTI, we have developed, tested and implemented two standard DTI pulse sequences that dedicated for TBI patients. One is temporal effective DTI pulse sequence that has a total scan time of less than 6 mins and another is more comprehensive DTI pulse sequence with a total scan time of approximately 15 mins. Thirty and sixty diffusion directions have been used for the short and long DTI pulse sequences, respectively. Below is the details of imaging parameters for the two standard DTI pulse sequences:

(A) DTI pulse sequence with 30 diffusion gradient directions: TR/TE = 11097/54 ms, FA = 90°, b = 1000 s/mm². Seventy axial slices, FOV = 240 x 240, matrix = 108 x 108, voxel size = 2.22 x 2.22 x 2.22 mm³, reconstructed to 1 x 1 x 2.22 mm³. Total scanning time is 6 minutes 51 seconds. Five averages for b=0 image.

(B) DTI pulse sequence with 60 diffusion gradient directions: TR/TE = 12761/54 ms, FA = 90°, b = 1000 s/mm². Seventy axial slices, FOV = 240 x 240, matrix = 108 x 108, voxel size = 2.22 x 2.22 x 2.22 mm³, reconstructed to 1 x 1 x 2.22 mm³. Total scanning time is 15 minutes 6 seconds. Ten averages for b = 0 image.

3. More advanced DTI pulse sequences have been developed. One is motion-insensitive pulse sequence that will help to resolve the potential problem associated with the TBI patient motion during MRI scans. Another is three dimensional DTI pulse sequence based on fast spin echo data acquisition strategy that will be able to obtain extremely higher spatial resolution (less than 1 mm in three directions). Both advanced pulse sequences have been implemented in our Philip 3T MRI scanner at the University of Chicago and the in vivo human subjects data shows these techniques have great advantages compared with the routinely used DTI sequences. We have finished the manuscript writing for these two advanced pulse sequences. One is under revision in the Journal of Magnetic Resonance Imaging and another will be submitted to NeuroImage. These two manuscripts are attached in this report.

Overall, the MRI physics development in this project has made satisfactory progress for the last two years. In the next year, we will complete the work on phantom testing and implement the standard DTI pulse sequences for the evaluation of TBI patients in clinical sites. The testing of reproducibility will be done using our approved human study protocol with manufacturer-supplied and our novel pulse sequences for data acquisition.

This work has been performed through the effort of our post-doctoral research associate, Ashish A. Tamane, Ph.D. under the direction of Prof. Jia-Hong Gao. Recently, Dr. Tamane was offered a position in industry and departed on 30 September 2011. His replacement in this position is pending. We are grateful to Dr. Tamane for his efforts and will miss him. We wish him success in his future professional activities and enjoy a warm and collegial long term relationship. Dr. Tamane has expressed his gratitude for the opportunity provided to work on this project.

Challenges

Among the most important challenges that we faced this year were Dr. Vannier's illness and rehabilitation resulting in an unavoidable and unexpected delay. After recovery, IRB approval had expired and reinstatement was required. The principal collaborator, Dr. Deborah Little from the University of Illinois-Chicago departed and has taken a new position at the Scott & White Clinic, VA Medical Center and Texas Tech University in Waco, Texas. The MRI physics post-doctoral research associate, Dr. Ashish Tamane has taken a new position in industry and should be replaced. Rebudgeting authority to engage the University of Chicago – Argonne National Laboratory Computation Institute required several months for review and approval so the software development process for a traumatic brain injury image repository could be done. Finally, the diffusion phantom received from Brain Innovation BV, Maastricht, NL was damaged in shipping and required a complex repair procedure that continues to date.

Next Funding Period

The goals for the next year include preparations for a sponsored workshop of D-MRI software toolbuilders who should undertake the analysis of TBI datasets and evaluation of the results. To accomplish this, a suitable on-line archive is required to manage data distribution and results collection. In preparation for evaluation of various software tools, we plan to take D-MRI of TBI datasets from studies published in the peer-reviewed literature and place them in the repository. Software tools have been downloaded and installed on local host computers which are capable of implementing the measurements used in the published studies. Having access to the datasets and automated tools will enable us to independently reproduce the results from the publications. Comparison of the published and independently processed data will allow us to verify the reports. If there are discrepancies, the root cause will be sought.

The independent verification of reported results in TBI clinical studies has not been done. However, in other areas of biomedicine, such independent analysis is considered important and valuable. (5) For example, in gene expression analysis, a new area of subspecialization

has emerged known as “Forensic Bioinformatics” as a result of work done by Keith Baggerly and associates at M.D. Anderson Cancer Center. (6, 7)

We anticipate that one contribution of our project will be to establish a mechanism and demonstrate the feasibility of independent verification for D-MRI of TBI studies. The effort required to accomplish this can also provide an automated infrastructure to simplify and aid in standardization of TBI clinical studies. An objective comparison of the performance in various software tools developed for D-MRI of TBI post-processing can be made using this infrastructure.

Recognizing that new TBI common data elements are available, they need to be implemented and tested in clinically realistic environment. Doing so, we can determine, 1) Are they sufficient? 2) Are they practical? Practical use of the CDEs will encourage their widespread adoption.

We expect to be able to test phantoms and human volunteers on all 3 major MRI scanner platforms where we use the “recommended” protocol from our June 2010 workshop. In this, we can test immediate and short term reproducibility within and between platforms. Evaluation of candidate phantoms (existing and new) will be done. The organization and presentation of a multi-institutional post-processing workshop focused on practical tools for TBI data processing of D-MRI scans is unprecedented. To accomplish this we need data sets and must have formal evaluation tool(s). We can thereby test the infrastructure for multi-site image analysis and data quality control.

Several multicenter TBI imaging projects are underway or planned, but not all are documented in clinicaltrials.gov. We intend to reach out and contact / visit as many as possible to inform them of roadmap workshop results and engage them in the process.

KEY RESEARCH ACCOMPLISHMENTS:

In the second year, we were able to complete the following:

1. Rebudgeting authority was obtained and effort was allocated among experts in imaging databases at the Computation Institute (U-Chicago & Argonne National Laboratory). Planning for implementation of the on-line traumatic brain injury database is underway.
2. Dr. Tamane, post-doctoral research MRI physicist has departed and will be replaced.
3. Dr. Deborah Little departed from UIC and a new subcontract to continue the work will be needed with her new institution in Texas.
4. Two research publications on D-MRI data acquisition methods were written and they have been submitted for publication.
5. A D-MRI phantom was received and has been repaired for use in human studies of D-MRI reproducibility.
6. A website for results dissemination has been created and populated with workshop materials (June 2010). <http://tbi.ci.uchicago.edu/>
7. In preparation for experiments conducted using phantoms and human volunteers to evaluate sources of variability and stability in MRI scanners and to validate the longitudinal evaluation of traumatic changes in brain white matter using diffusion MRI (D-MRI), we re-applied and completed the necessary IRB and HRPO review processes to gain approval so this work can commence.

REPORTABLE OUTCOMES:

1. Ashish A. Tamhane, Xiaodong Guo, Yonghua Xu, Lixia Yang, Bin Chen, Michael Vannier, Jia-Hong Gao. 3D Trajectory of ROtating Planes using Fast spin Echo (3D TROPFE) for Isotropic Sub-millimeter Resolution Diffusion Tensor Imaging.
2. Ashish A Tamhane, Konstantinos Arfanakis, Mark Anastasio, Xiadong Guo, Michael Vannier, Jia-Hong Gao. Rapid Data Acquisition for PROPELLER-MRI: A Combination of Iterative Reconstruction and Under-Sampling

CONCLUSION:

Diffusion MRI of neurological/neuropsychiatric disorders (chronic TBI, PTSD, and related disorders) is an important potential market for the imaging industry. Virtually all individuals with traumatic brain injuries – including all ages are potential candidates – whether injury is due to auto, sports, combat, falls or other. Serum protein changes after trauma, optical imaging methods, PET/SPECT with radioisotope agents, and other technologies are less generally available or have known limitations. No “one size fits all”, given the diversity of patients and injuries. By preparing the infrastructure needs and facilitating interactions among diverse experts in TBI and related disciplines, the translation of promising D-MRI technology into clinical practice based on a solid body of evidence can be accomplished.

REFERENCES:

1. Federal Interagency Traumatic Brain Injury Research (FITBIR) database, August 29, 2011, <http://www.nih.gov/news/health/aug2011/ninds-29.htm>
2. The National Database for Autism Research, <http://www.hhs.gov/open/initiatives/hhsinnovates/round3/ndarpage.html>
3. Aaron Saenz. Database for autism holds hope for answers, treatments. <http://singularityhub.com/2010/02/11/database-for-autism-holds-hope-for-answers-treatments/>
4. Pim Pullens, Alard Roebroek, Rainer Goebel, *Ground truth hardware phantoms for validation of diffusion-weighted MRI applications*, Journal of Magnetic Resonance Imaging. Volume 32 Issue 2, Pages 482 – 488.
5. Rabiya S.Tuma. Calls for New Reporting Standards, Quality Control in Microarrays. JNCI Vol. 102, Issue 18, September 22, 2010, 1380-1.
6. Keith A. Baggerly and Kevin R. Coombes. Deriving chemosensitivity from cell lines: forensic bioinformatics and reproducible research in high-throughput biology. Annals of Applied Statistics. 3(4):1309-1334, 2009.
7. Baggerly K. Disclose all data in publications. Nature 467(7314):401, 9/2010. PMID: 20864982.

APPENDICES:

1. 3D trajectory of rotating planes using fast spin echo (3d TROPFE) for isotropic sub-millimeter resolution diffusion tensor imaging.
2. Rapid data acquisition for propeller-MR MRI: a combination of iterative reconstruction and under-sampling.
3. Diffusion MRI phantom

**3D Trajectory of ROTating Planes using Fast spin Echo (3D TROPFE) for
Isotropic Sub-millimeter Resolution Diffusion Tensor Imaging**

**Ashish A. Tamhane¹, Xiaodong Guo¹, Yonghua Xu², Lixia Yang², Bin Chen³,
Michael Vannier¹, Jia-Hong Gao¹**

Brain Research Imaging Center and Department of Radiology,

The University of Chicago, Chicago, IL

Department of Radiology, Xuhui Central Hospital of Shanghai and
Chinese Academy of Sciences Shanghai Medical Center, Shanghai, China

³Purdue University

Corresponding Author:

Jia-Hong Gao, Ph.D.

Brain Research Imaging Center

The University of Chicago

5841 South Maryland, MC 2026

Chicago, IL 60637

Tel: 773-834-0480

Fax: 773-834-7610

E-mail: jgao@uchicago.edu

Funding Sources: DOD W81XWH-09-2-0102

Manuscript word count: 3591

Keywords: Sub-millimeter resolution, DTI, 3D Projection Reconstruction

ABSTRACT

Traditionally, DTI data are collected using single shot spin echo echo planar imaging (SS SE-EPI), in which image resolution was restricted by T_2 decay and also images suffer from severe susceptibility related artifacts near the air-bone-tissue interface. Because of low resolution, many details in underlying white matter fiber tracts are lost. Hence, it is desirable to develop acquisition technique, which is less sensitive to susceptibility artifacts but can produce higher resolution diffusion weighted images. Previously, multi-shot fast spin echo (FSE) sequence based radial 2D k-space trajectory was proposed for this purpose and sub millimeter isotropic voxel size was achieved. But wider refocusing RF pulses (at least 300% larger than slice of interest) were employed in this sequence to attain uniform B_1 field over very thin slice profile. This arrangement prohibited acquisition of adjacent slices within one scan session and requires at least three scan sessions to cover any region of interest. This prolongs imaging time could lead to serious errors caused by subject motion between scan sessions and also may cause discomfort to subject. This drawback of radial FSE 2D DTI acquisition was addressed in this study with use of 3D TROPFE sequence. Because of 3D nature of k-space sampling, adjacent slices can be acquired in one scan session with proposed method. Images were reconstructed using magnitude filtered back projection to eliminate shot-to-shot phase variation. The resulting images are free from susceptibility distortions because of FSE acquisition, less sensitive to partial volume effects because of high resolution and high SNR because of 3D acquisition. Results are demonstrated in brain images of normal human volunteers.

1. INTRODUCTION

Diffusion Tensor Imaging (DTI) is a MR imaging technique that enables *in vivo* measurement of anisotropic diffusion of water in human brain white matter to produce fiber tract images (Basser et. al., 1994). DTI has been instrumental in diagnosis of several diseases associated with human brain white matter degeneration such as Alzheimer (Bozzali et. al., 2002; Medina et. al., 2008), Multiple Sclerosis (Commowick et. al., 2008; Filippi et. al., 2001) and diffuse axonal injuries caused by severe trauma (Arfanakis et. al., 2001). DTI is also proving to be an important pre-surgical planning tool for neurosurgeons (Romano et. al., 2009).

Traditionally, DTI data are collected using single shot spin-echo echo-planar imaging (SS SE-EPI), which is sensitive towards distortions caused by B_0 inhomogeneity near air-bone-tissue interface called as susceptibility artifacts. Due to T_2^* decay, SS SE-EPI is also severely limited in terms of resolution and typically voxel size larger than 1.8^3 mm^3 was reported in previous DTI studies. Hence, diffusion weighted signal from a single voxel in human brain is a mixture of microscopic diffusion weighted signals from the complex microstructure of white matter (Basser and Pierpaoli, 1996; Alexander et. al., 2001; Tuch et. al., 2002). In case of SS SE-EPI, further decrease in voxel size or increase in resolution results in longer EPI readout time, which would increase susceptibility related distortions as well as significant decrease in SNR. Hence, it is highly desired to develop a better acquisition and reconstruction technique to obtain high-resolution diffusion weighted images with less susceptibility artifacts and higher SNR.

From clinical point of view, high resolution DTI will provide more insight into white matter alterations in neuro-degenerative diseases particularly in the region where SS SE-EPI has limited success because of susceptibility artifacts and partial volume effects. For example, significant changes in trace and Fractional Anisotropy (FA) values have been observed in the region of medial temporal lobe, hippocampus and entorhinal cortex for Alzheimer patients, when compared to normal subjects (Arfanakis et. al., 2007). These regions are sensitive to susceptibility artifacts and cannot be easily identified by SS SE-EPI. Similarly, optic chiasm is challenging structure to image with SS SE-EPI DTI, because of its small size and proximity towards air/tissue interface, blood vessel and cerebrospinal fluid. This structure is associated with various intrinsic pathologies such as multiple sclerosis, optic neuropathy and gliomas.

Early stages of these pathologies are hard to diagnose with any conventional contrast agent but may induce changes in FA because of changed fiber pathways. Proposed method would allow understanding of change in anatomy of underlying white matter structures in such regions and will provide a powerful tool for diagnosis of such elusive diseases.

Recently, it was demonstrated that sub-millimeter isotropic resolution for DTI could be achieved with radial FSE sequence (Sarlls and Pierpaoli, 2009). However, in this technique, a slice thickness for refocusing RF pulse was increased to 300% of excitation slice thickness to improve B_1 inhomogeneity within thin slice. As a result, adjacent slices could not be acquired in one scan session and at least three scanning sessions were required to cover region of interest (ROI) (Sarlls and Pierpaoli 2009). This increased imaging time could induce errors because of change in subject's position between different scan sessions.

These shortcomings could be addressed by use of 3D k-space trajectory, which also has added advantage of higher SNR when compared with 2D sequences. Recently, 3D FSE variable density spiral (VD spiral) trajectory with iterative reconstruction technique was proposed (Frank et. al., 2010). Similarly, a steady state diffusion weighted sequence based on 3D-Projection Reconstruction (3D-PR) trajectory was developed (McNab et. al., 2010). In both methods, images were reconstructed using conventional gridding (Jackson et. al., 1991). However, both techniques did not demonstrate the capability to breach barrier of sub millimeter isotropic voxel size *in vivo* using of 3T scanner.

Previously, Alexander et. al (1999) introduced 3D projection reconstruction trajectory for k-space sampling using FSE and combined it with magnitude filtered back projection (mFBP). This acquisition and reconstruction technique has potential to achieve sub-millimeter resolution using FSE. However, it has never been extended to acquire diffusion weighted images. The difficulty of DWI/DTI with FSE has been discussed in details previously (Mori and van Zijl, 1998; Pipe et. al., 2002; Sarlls and Pierpaoli, 2008). Major obstacle for using FSE technique to acquire diffusion weighted images is violation of Carr-Purcell-Meiboom-Gill (CPMG) condition (Meiboom and Gill, 1958). The CPMG condition requires initial phase of transverse magnetization and phase of RF refocusing phase to be same for successful FSE imaging. But

after application of diffusion gradients in FSE, spins in transverse plane are left with random spatially varying phase (Pipe et. al., 2002; Sarlls and Pierpaoli, 2008). This may results in sever echo attenuation within echo train in FSE sequence.

In this study, 3D PR FSE sequence was implemented to incorporate diffusion gradients to obtain the isotropic sub-millimeters resolution in DTI at 3T. The violation of CPMG condition was tackled by phase cycling introduced by Pipe et. al.,(2002). Image reconstruction using mFBP, have been useful particularly to reconstruct diffusion weighted images to remove shot to shot phase variation. Similarly, this reconstruction is also less sensitive to motion related artifacts.

The whole image acquisition and reconstruction method will be referred as 3D Trajectory of Rotating Planes using Fast spin Echoes (TROPFE)-DTI in further study. Proposed method would acquire DTI data with sub-millimeter resolution in one scan session as opposed to three scan sessions required by 2D radial FSE. This advantage will make sub millimeter resolution DTI clinically more viable. Also, it will provide more insights into organization of complex white matter structures and will open new avenues in diagnosis of neuro-degenerative diseases.

2. MATERIALS AND METHODS

2.1 DATA ACQUISITION

The trajectory proposed in this study acquired data along a set of parallel lines passing through center of k-space. This set of lines is referred as “blades” in this study. The echo train is modulated along z/slice-encoding (Alexander et. al., 1999) and as a result, with one excitation one projection plane in 3D k-space was covered. The entire 3D k-space is covered by uniformly increasing projection angle for every excitation. The trajectory was described previously as 3D TROPFE in reference (Alexander et. al., 1999) and used for T_2 weighted imaging but was not extended for DTI application.

Robust FSE imaging typically requires initial phase of transverse magnetization and phase of RF refocusing pulse to be same, which is known as CPMG condition. When large amplitude diffusion-weighted gradients are embedded to FSE sequence, transverse magnetization is left with a spatially varying and unknown phase. This violation of CPMG condition can cause rapid decay in signal magnitude depending upon starting phase of transverse magnetization (Pipe and

Farthing, 2002) in 2D as well as 3D sequences. To counter this problem, a mixed-CPMG phase cycling method was implemented in which, phase of refocusing RF (180^0) pulse was alternated between x and y axes i.e. $\{180^0_x-180^0_y-180^0_x-180^0_y\}$. This produced fairly stable diffusion weighted signal. The spin evolution with phase cycling was demonstrated in Figure 1. However, phase offset between even and odd echoes remained an issue with use of a multiple channel receiver coil (Pipe et. al., 2002). Before reconstruction data from every other even echo were multiplied by “-1”, so all even echoes have similar phase. Same operation was performed on odd echoes. A zero-order phase correction was performed on each FSE blade, same as triangular window correction performed in PROPELLER DWI (Pipe et. al., 2002; McNab et. al., 2010). This correction was intended to remove the effects of rigid body shifts from diffusion weighted images as well as any absolute phase difference between data from even and odd echoes. After this step, data from even and odd echoes were added.

2.2 IMAGE RECONSTRUCTION

A reconstruction was performed in different way by taking advantage of geometry of k-space trajectory. One dimensional FFT was calculated along z-direction and then images were obtained using mFBP algorithm to remove shot-to-shot phase variation as explained in reference (Trouard et. al., 1999). The use of mFBP has helped to minimize motion related artifacts in diffusion weighted images (Trouard et. al., 1999). This method of reconstruction was previously described in reference (Alexander et. al., 1999; Peters et. al., 2000) but in this study, a phase correction with triangular window (Pipe et. al., 2002) was incorporated for diffusion imaging. . Because of 3D acquisition, a 3D inverse Fourier transform needed to be performed on acquired data to reconstruct images. In case of Cartesian sampling, it can be achieved using 3D inverse Fast Fourier Transform (3D IFFT). But, non-Cartesian nature of 3D TROPFE trajectory prohibited direct use of 3D IFFT operation. However, in this trajectory, data along z-axis lies along Cartesian grid. Also, 3D inverse operation can be divided into three 1D IFFT along each direction. Taking advantage of this geometrical feature of trajectory, 1D IFFT was performed along z-direction on acquired k-space data (Figure 2(a)). This results in 2D Projection Reconstruction k-space, which is then rearranged along polar co-ordinates (r, θ) (Figure 2(b)). Second 1D IFFT operation was performed on data on polar grid along θ for each slice, which

results in sinogram for each slice (Figure 2(c)). From these data, images are reconstructed using mFBP algorithm (Trouard et. al., 1999) (Figure 2(c)).

2.3 PHANTOM EXPERIMENTS

To test accuracy of diffusion measures, experiments were performed on phantom, which is a bottle, filled with tap water at room temperature (77F). Data for phantom were collected in the Brain Research Imaging Center at the University of Chicago on a 3T Philips Achieva scanner (Philips Healthcare Inc., Best, Netherlands) with maximum gradient strength of 40 mT/m. Six direction diffusion weighted datasets with $b = 1000 \text{ s/mm}^2$ and one $b = 0$ data were acquired using 3D TROPFE sequence. The “Overplus” gradient sampling scheme was used to obtain diffusion weighted data (Tijssen et. al., 2009). This scheme combines available gradient power along more than one axis to produce stronger diffusion weighting and shorter echo time (TE) when compared with conventional unit-sphere sampling. A standard 8-channel head coil was used for data acquisition. Total imaging time was 50 minutes. Data were acquired with following acquisition parameters: TR/TE = 1200 ms/47 ms, slab thickness = 5.4 mm, ETL = 12, FOV = 230 mm x 230 mm, number points in readout = 256, number of projections = 360, angle between projections = 0.5° . Slab selective refocusing pulses were used during acquisition. Images were reconstructed using mFBP reconstruction as described previously (Alexander et. al., 1999). Mean ADC maps were calculated for phantom data.

Next experiment was designed to demonstrate signal attenuation caused by CPMG violation and subsequent improvements achieved by phase cycling in 3D TROPFE. All phase encoding gradients were turned off during acquisition so that center of k-space could be acquired with each spin echo. Data were acquired using 3D TROPFE DTI sequence with above mentioned protocol for water phantom. The magnitude of spin echoes were plotted against echo train length for $b = 0$ and $b = 1000 \text{ s/mm}^2$, with and without phase cycling.

2.4 HUMAN EXPERIMENTS

To verify 3D TROPFE DTI sequence for *in-vivo* sub-millimeter resolution data, four healthy male volunteers were scanned using above mentioned acquisition parameters. Cardiac gating was

not applied during acquisition. Subjects were asked to keep head steady to avoid any rigid body motion related artifacts.

3. RESULTS

3.1 PHANTOM EXPERIMENTS

Figure 3 shows ($b = 0$ and $b = 1000 \text{ s/mm}^2$) images of phantom. Each row in Figure 3 corresponds to different slices, while each column represents images from different gradient encoding. Mean ADC maps were obtained from these data are shown in last column. Mean ADC value for phantom was observed to be $2.05(\pm 0.2) \times 10^{-3} \text{ mm}^2/\text{s}$. Figure 4 shows effect of phase cycling on diffusion weighted signal in FSE. Graphs in Figure 4(a) are obtained when no diffusion gradients were applied ($b = 0$). The solid and dashed lines correspond to data with and without phase cycling, respectively. Figure 4(b) represents same graphs with diffusion gradients turned on ($b = 1000 \text{ s/mm}^2$). For $b = 0$, CPMG condition was not violated and signal reduction was governed by T_2 decay. Hence, no significant difference was observed between signal obtained with and without phase cycling. However, for $b = 1000 \text{ s/mm}^2$, after application of diffusion gradients, spins in transverse plane are left with random phase. This condition does not satisfy CPMG requirement, which states that initial phase of transverse magnetization and refocusing RF should be same. This results in rapid signal magnitude decay along ETL (Figure 4(b) - dashed line). This decay was curbed by using phase cycling as shown with solid line in Figure 4(b).

3.2 HUMAN EXPERIMENTS

Figures 5 show images of brain of typical human subject acquired with 3D TROPFE DTI sequence. SNR in ($b = 0$) images was measured in ROI of corpus callosum and was found to be equal to approximately 20. SNR was defined as the mean of signal divided by signal standard deviation. Last column in image shows corresponding mean ADC maps for each slice. A total of six consecutive slices of data were acquired. Mean ADC value in white matter region of frontal lobe was observed to be $0.75(\pm 0.5) \times 10^{-3} \text{ mm}^2/\text{s}$. Figure 6 shows FA maps and color coded FA maps calculated from isotropic sub-millimeter resolution diffusion weighted images. Very high resolution features were observed FA and colormaps obtained from 3D TROPFE DTI sequence.

4. DISCUSSIONS

In phantom studies, even in presence of water-air interface, no significant distortions caused by susceptibility artifacts were observed (Figure 3). Estimated mean ADC values were in agreement with previous study (Sarlls and Pierpaoli, 2008). Similarly, for human brain data, mean ADC (Figure 5) values observed in frontal lobe white matter region in also in agreement with previously published results (Hellenius J et. al., 2002).

FA and color coded FA maps (Figure 6) obtained from in-vivo data shows similar fiber orientation when compared with previous DTI literature but with very high resolution. Main purpose of this study was to demonstrate feasibility of 3D FSE sequence to achieve sub-millimeter isotropic resolution, which has been successfully achieved. But, it is also required to compare this sequence with other sequences such as clinically available SS SEEPI and other 3D DTI sequences such as 3D DW VDS RARE (Frank et. al., 2010) or TURBINE (McNab et. al., 2010). This is one of the undergoing projects in our laboratory.

Also, human brain diffusion weighted images are appeared to be not affected by cardiac pulsation in this study. However, this effect may be more visible near region which experience strong pulsatile motion such as brainstem. These potential artifacts can be minimized with use of cardiac gating at the cost of increased imaging time. McNab et. al. (2010) recently proposed a self navigation technique for similar trajectory, which can minimize effects of non-rigid body motion on diffusion weighted images. However, this subject requires very detailed investigation and will be explored in future publications.

Previously, non-Cartesian 2D FSE/GRASE/EPI DTI sequences have been developed to achieve high in-plane resolution (Pipe et. al., 2002; Wang et. al., 2005; Pipe and Zwart, 2006; Skare et. al., 2006; Holdsworth et. al., 2009). However, because of inherent SNR limitations of 2D acquisition and B_1 inhomogeneity, slice thickness could not be reduced beyond 3 mm. An isotropic sub-millimeter resolution in DTI using FSE based sequence at 3T was achieved using 2D radial trajectory (Sarlls and Pierpaoli, 2009). In general, in FSE DTI sequence, imperfect 180° pulse caused significant drop in diffusion weighted sequence and very thin slice profile further complicated this issue. However, Sarlls et. al., (2009) addressed this problem by

applying 300% wider slice profile for 180° refocusing RF pulses to improve B_1 uniformity very thin slice under consideration. But this technique has necessitated a gap of at least two slices between consecutive slices in one scan session. As a result, at least three scan sessions were required to cover entire region of interest, which increased its imaging time by three folds. This could also introduce significant errors caused by different positions of same subject in different scan sessions and would hamper intra-subject repeatability for very small anatomical structures as optic chiasm. Hence, even though 2D radial FSE DTI has great potential to discover exact fiber ordering of very small anatomical structures with sub-millimeter resolutions, it is severely limited in terms of clinical applicability because of imaging time and requirement of multi-session scanning. 3D TROPFE DTI sequence reported in this present study was precisely designed to address these drawbacks of 2D radial FSE sequence. 3D k-space sampling of this sequence allows acquisition of consecutive slices in one scan session. However, resolution along z-encoding has been affected by T_2 decay in echo train. This has also limited number of spin echoes in echo train.

Imperfections in 180° slice profile can cause significant signal decay in any FSE based DTI sequence depending on random phase produced by diffusion gradients at the start of ETL. This could lead to violation of CPMG condition, which is typically handled by phase cycling in previous studies. In 3D TROPFE DTI sequence also, phase cycling was employed to counter signal decay caused by non-CPMG condition. As demonstrated in Figure 4, phase cycling has successfully improved signal decay for ETL of twelve in 3D TROPFE sequence. However, it could not remove variations in magnitude and phase between even and odd echoes in diffusion weighted signal caused by non-CPMG condition. Hence, it was required to separate data from even and odd echoes. The phase correction method (Pipe et. al., 2002) employed, also removed any absolute phase difference between even echo and odd echoes before combining k-space data. However, separation of even and odd echoes have reduced effective slab thickness and increased redundant sampling. In future, we plan to sample orthogonal blades or projections with even and odd echoes, separately, which is very similar process described as split-blade in turbo-prop (Pipe and Zwart, 2006). This will enable sampling of two blades per excitation/TR and will reduce number of excitations/TRs required to cover entire k-space by two. This reduced imaging time

can be utilized further to acquire diffusion weighted images from more directions to decrease noise in calculated tensors.

The number of projections in this trajectory was empirically decided to be 360. Each projection takes one TR of imaging time. Hence, number of projections is directly proportional to imaging time. But, reduction in number of projections could lead to blurring or smoothing in image space. However, least square reconstructions or compress sensing image reconstruction technique can be applied to this trajectory to further reduce imaging time. Also, data for multiple slabs in one TR could be acquired, which could lead to increase FOV in z-direction and will increase clinical applicability of proposed acquisition.

Recently, sub-millimeter resolution in DTI have been achieved at field strength of 7T using a combination of 2D reduced FOV EPI and parallel imaging using GRAPPA technique (Calamante et al., 2011). However, 1 mm isotropic resolution was only possible with this technique because of necessary high SNR achievable at 7T field strength. If similar technique was applied at 3T then resolution was restricted to 2.5mm x 2.5 mm x 2.5 mm (Calamante et. al., 2011). Considering 7T MRI scanner are higher costs and not widely available, the novel technique developed in this study in obtaining 3D higher resolution DTI at 3T will be able to distribute and serve well to urgently clinical needs to medical community.

Previously, high angular resolution diffusion imaging (HARDI) acquisition methods (Frank 2001; Tuch et. al., 2002; Jackson and Alexander, 2003; Ozarslan and Mareci, 2003; Tourier et. al., 2004) and diffusion spectrum imaging (DSI) (Wedeen et. al., 2005) have all been proposed to understand complex architecture of white matter. All these techniques have demonstrated ability to uncover multiple fiber crossing within a single voxel but still lacks ability to provide precise location of fibers within voxel. These methods used SS SE-EPI to acquire data and have approximately 2.5 mm isotropic image resolution. In contrast, proposed method would enable DTI acquisition with 0.9 mm isotropic resolution and would provide better localization of very complex and highly heterogeneous organization of fibers in small white matter structures.

5. CONCLUSIONS

In this study, a 3D FSE based multi-shot acquisition method, 3D TROPFE was presented to achieve a sub-millimeter isotropic resolution in DTI. Being based on FSE sequence, it is less sensitive to susceptibility artifacts caused by B_0 inhomogeneity. Data were obtained using 3D projection reconstruction trajectory and images were reconstructed from k-space using magnitude FBP reconstruction to minimize shot-to-shot phase variation in FSE based diffusion weighted sequence. Since, in this method, echo train was modulated along z-direction, T_2 decay imposed restriction on resolution along that direction as well as on slab thickness. But, when compared with existing 2D technique, proposed method provides advantages of higher SNR and ability to acquire consecutive slices in one scan session. As in case of any multiple spin echo diffusion weighted sequence, phase cycling method was employed to reduce signal attenuation caused by violation of CPMG condition. Separation of even and odd echoes was performed to mitigate effects of phase discontinuity between them, which increased redundancy in k-space sampling and further reduced slab thickness. Effects of cardiac pulsation on data acquired with this method needed to investigate in detail, which is subject of future research. In conclusion, proposed combination of acquisition and reconstruction would be extremely useful to understand complex and heterogeneous fiber organization in small white matter structure and will provide opportunities for early detection and diagnosis of very elusive white matter related diseases.

REFECERENCE

- Alexader AL, Hasan KM, et. al., 2001. Analysis of partial volume effects in diffusion tensor MRI. *Magn Reson Med*, 45(5), 770-780.
- Alexander AL, Roberts J, et. al., 1999. MR imaging with 3D fast spin echo using projection reconstruction technique description and applications. *IEEE Nuclear Science Symposium, Conference Record 2*, 1087-1090.
- Arfanakis, K. Haughton VM, et. al., 2002. Diffusion tensor MR imaging in diffuse axonal injury. *Am J Neuroradiol*, 794-802.
- Arfanakis K, Gui M, et. al., 2007. Investigating the medial temporal Lobe in Alzheimer's disease and mild cognitive impairment, with turboprop diffusion tensor imaging, MRI-volumetry, and T 2-relaxometry. *Brain Imaging and Behavior*, 1, 11-21.
- Basser PJ, Mattiello J, et. al., 1994. Estimation of the effective self-diffusion tensor from the NMR spin echo. *J Magn Reson*, 103, 247-254.
- Basser PJ, Pierpaoli C, 1996. Microstructural and physiological features of tissues elucidated by quantitative-diffusion-tensor MRI. *J Magn Reson*, 111, 209-219.
- Bozzali M, Falini A, et. al., 2002. White matter damage in Alzheimer's disease assessed in vivo using diffusion tensor magnetic resonance imaging. *J of Neurol Neurosurg Psychiatry*, 72, 742-746.
- Calamante F, Tournier J-D, et. al., 2011. Track density imaging (TDI): validation of super resolution property. *NeuroImage*, 56(3), 1259-1266.
- Commowick O, Fillard P, et. al., 2002. Detection of DTI white matter abnormalities in multiple sclerosis patients. *Med Image Comput Comput Assist Interv*, 11, 975-982.
- Filippi M., Cercignani M, et. al., 2001. Diffusion tensor magnetic resonance imaging in multiple sclerosis. *Neurology*, 56, 304-311.
- Frank LR, 2001, Anisotropy in high angular resolution diffusion-weighted MRI. *Magn Reson Med*, 45(6), 935-939.
- Frank, LR, Jung Y, et. al., 2010. High efficiency, low distortion 3D diffusion tensor imaging with variable density spiral fast spin echoes (3D DW VDS RARE). *Neuroimage*, 49, 1510-1523.
- Helenius J, Soinne L, et. al., 2002. Diffusion weighted MR imaging in normal human brains in various age groups. *AJNR*, 23, 194-199.

- Holdsworth SJ, Skare S, et. al. 2009. Robust GRAPPA-accelerated diffusion-weighted readout-segmented (RS)-EPI. *Magn Reson Med*, 62, 1629-1640.
- Jackson JJ, Meyer CH, et. al., 1992. Selection of a convolution function for Fourier inversion using gridding. *IEEE Trans Med Imaging*, 10, 473-478.
- Jansons KM, Alexander DC, 2003. Persistent angular structure: new insights from diffusion magnetic resonance imaging data. *Inverse Problems*, 19(5), 1031-1046.
- Meiboom S, Gill D, 1958. Modified spin-echo method for measuring nuclear relaxation times. *Review of Scientific Instruments*, 29, 688.
- McNab JA, Gallichan D, et. al., 2010. 3D steady-state diffusion-weighted imaging with trajectory using radially batched internal navigator echoes (TURBINE). *Magn Reson Med*, 63, 235-242.
- Medina DA, Gaviria M, 2008. Diffusion tensor imaging investigations in Alzheimer's disease: the resurgence of white matter compromise in the cortical dysfunction of the aging brain. *Neuropsychiatr Dis Treat*, 4, 737-742.
- Mori S, van Zijl, PC, 1998. A motion correction scheme by twin-echo navigation for diffusion-weighted magnetic resonance imaging with multiple RF echo acquisition. *Magn Reson Med*, 40, 511-516.
- Ozarslan E, Mareci TH, 2003. Generalised diffusion tensor imaging and analytical relationships between diffusion tensor imaging and high angular resolution diffusion imaging. *Magn Reson Med*, 50(5), 955-965.
- Peters DC, Korosec FR, et. al., 2000. Undersampled projection reconstruction applied to MR angiography. *Magn Reson Med*, 43, 91-101.
- Pipe JG, Farthing VG, et. al., 2002. Multishot diffusion-weighted FSE using PROPELLER MRI. *Magn Reson Med*, 47, 42-52.
- Pipe JG, Zwart, N, 2006. TurboProp: improved PROPELLER imaging. *Magn Reson Med*, 55, 380-385.
- Romano A, D'Andrea G, et. al., 2009. Pre-surgical planning and MR-tractography utility in brain tumor resection. *Eur Radiol*, 19, 2798-2808.
- Sarlls JE, Pierpaoli C, 2008. Diffusion-weighted radial fast spin-echo for high-resolution diffusion tensor imaging at 3T. *Magn Reson Med*, 60, 270-276.

- Sarlls JE, Pierpaoli C, 2009. In vivo diffusion tensor imaging of the human optic chiasm at sub-millimeter resolution. *Neuroimage*, 47, 1244-1251.
- Skare S, Newbould RD, et. al., 2006. Propeller EPI in the other direction. *Magn Reson Med* , 55, 1298-1307.
- Tijssen RHN, Jansen JFA, et. al., 2009. Assessing and minimizing the effects of noise and motion in clinical DTI at 3T. *Human Brain Mapping*, 30, 2641-2655.
- Tournier JD, Calamante F, et. al., 2004. Direct Estimation of the fiber orientation density function from diffusion-weighted MRI data using spherical deconvolution. *Neuroimage*, 23 (3), 1176-1185.
- Trouard TP, Theilmann, et. al., 1999. High-resolution diffusion imaging with DIFRAD-FSE (diffusion-weighted radial acquisition of data with fast spin-echo) MRI. *Magn Reson Med*, 42, 11-18.
- Tuch DS, Reese TG, et. al., 2005. High angular resolution diffusion imaging reveals intravoxel white matter fiber heterogeneity. *Magn Reson Med*, 22(2), 302-306.
- Wang FN, Huang TY, et. al., 2005. PROPELLER EPI: an MRI technique suitable for diffusion tensor imaging at high field strength with reduced geometric distortions. *Magn Reson Med*, 54, 1232-1240.
- Wedeen VJ, Hagmann P, et. al., 2005. Mapping complex tissue architecture with diffusion spectrum magnetic resonance imaging. *Magn Reson Med*, 54(6), 1377-1386.

FIGURE CAPTIONS

Figure 1: Spin evolution with phase cycling is demonstrated in this figure. The figure 1(a) shows time series with RF pulses and spin echoes. Figure 1(b) shows, spin evolution for corresponding time in series. The phase of refocusing RF is alternated between x and y axes and every other even and odd echo produced phase difference of 180° . B_1 denotes applied RF pulse.

Figure 2: Image reconstruction process from 3D TROPFE technique is implemented in three steps. In first step (a), FFT was taken along z -encoding. In second step (b) data for each slice was reorganized into polar (r, θ) co-ordinate system. In last step (c), first FFT was taken along (θ) axis for each line of each slice and then images were reconstructed using magnitude FBP reconstruction.

Figure 3: Water phantom images acquired with 3D TROPFE DTI are shown. First column corresponds to $b = 0$ images while subsequent columns are diffusion weighted ($b = 1000 \text{ s/mm}^2$) images. All images have isotropic resolution of $0.9 \text{ mm} \times 0.9 \text{ mm} \times 0.9 \text{ mm}$. Total width of slab is 5.4 mm . Each row represents different slice profile. ADC maps of corresponding slices were shown in last column.

Figure 4: Signal magnitude of spin echoes was plotted against echo number in 3D TROPFE DTI acquisition for (a) $b = 0$ and (b) $b = 1000 \text{ s/mm}^2$. Solid and dotted lines represent signal acquired with and without phase cycling, respectively. For $b = 0$, signal obtained by both method did not show significant difference. In contrast, for $b = 1000 \text{ s/mm}^2$, signal acquired without phase cycling exhibited significant drop in magnitude for higher echo number when compared with signal obtained with phase cycling.

Figure 5: Human brain images acquired with 3D TROPFE DTI. First column corresponds to $b = 0$ images while subsequent columns are diffusion weighted ($b = 1000 \text{ s/mm}^2$) images. All images have isotropic resolution of $0.9 \text{ mm} \times 0.9 \text{ mm} \times 0.9 \text{ mm}$. Total width of slab is 5.4 mm . Average SNR of 20 was measured in various white matter region of slab. Effect of cardiac pulsation was not visible in any diffusion weighted image for slab. ADC maps of corresponding slices were shown in last column.

Figure 6: FA and color coded FA maps of human brain images obtained with 3D TROPFE DTI sequence and reconstructed using mFBP reconstruction (spatial resolution 0.9 mm x 0.9 mm x 0.9 mm).

Figure 1

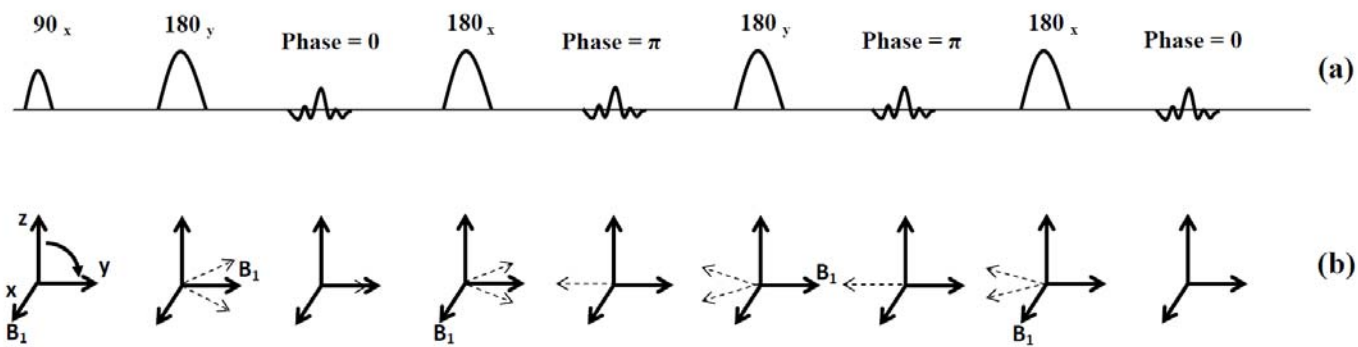


Figure 2

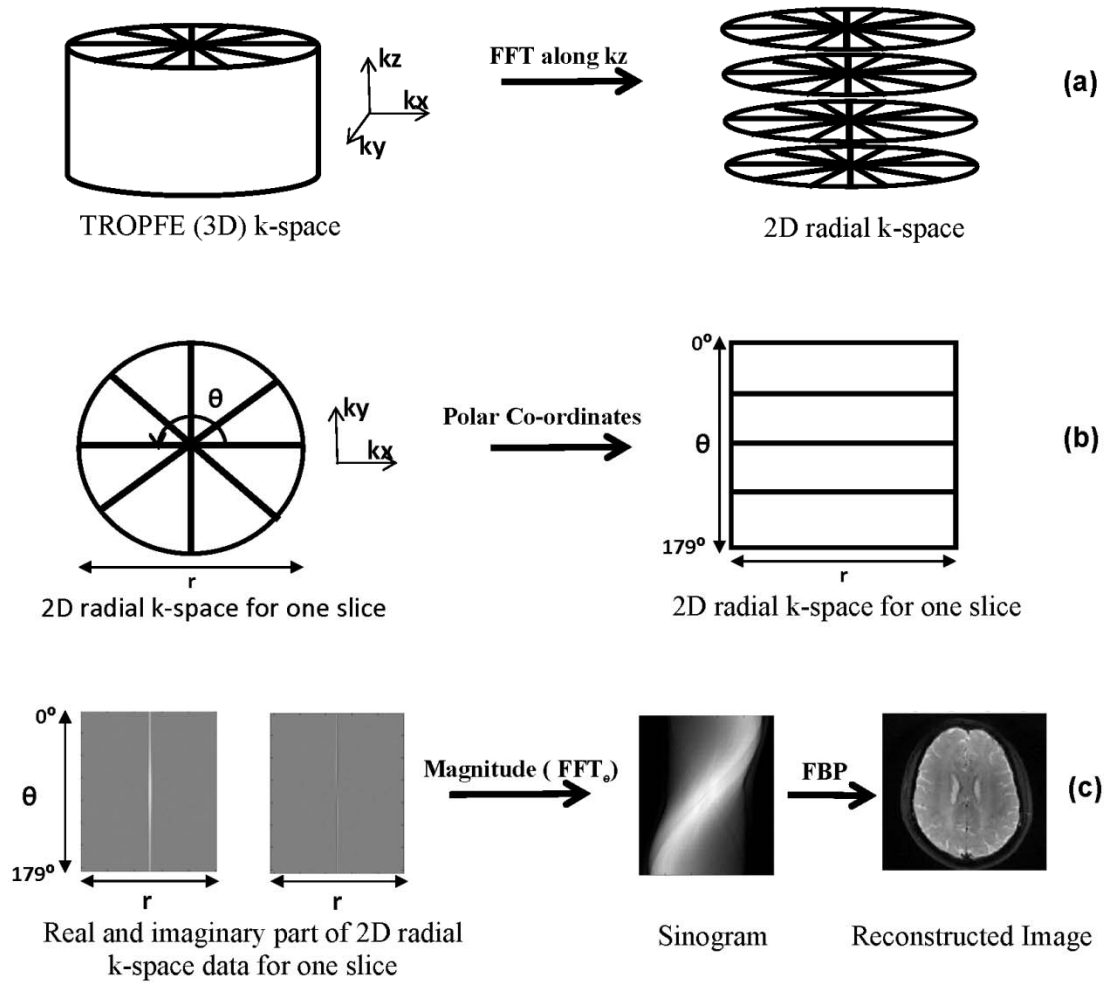


Figure 3

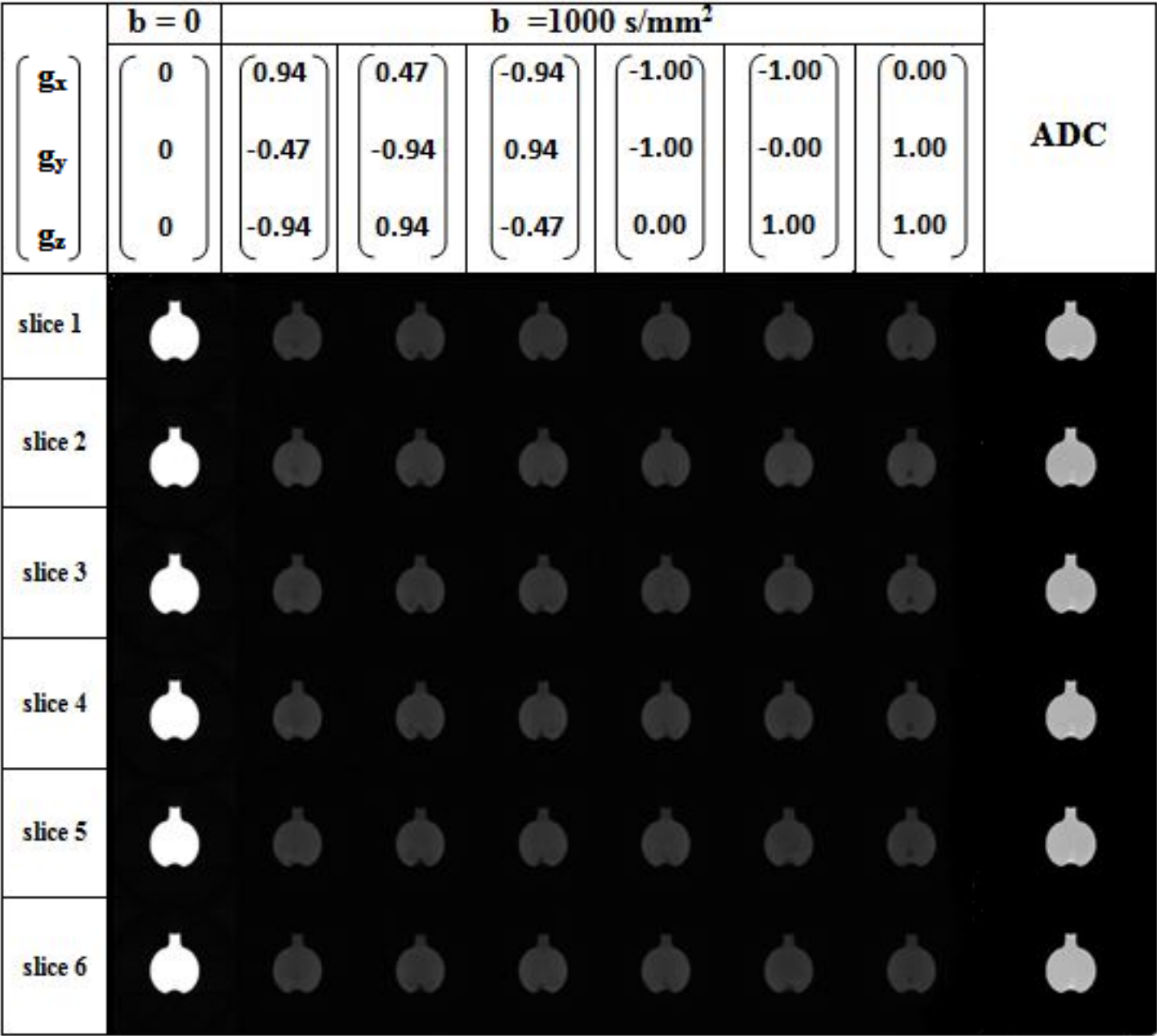


Figure 4

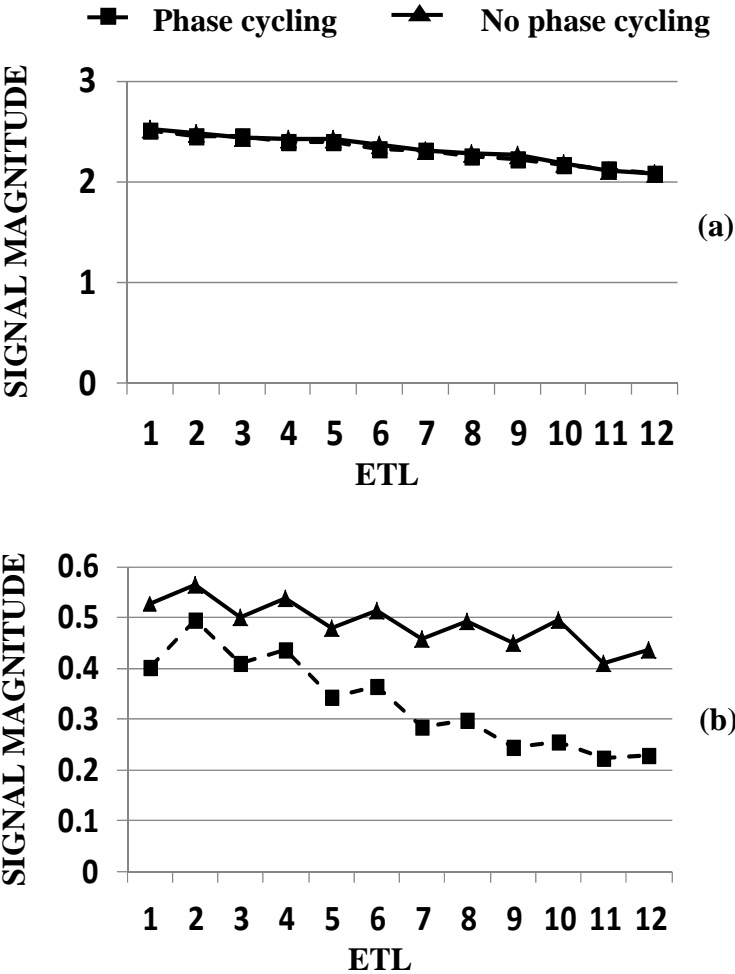


Figure 5

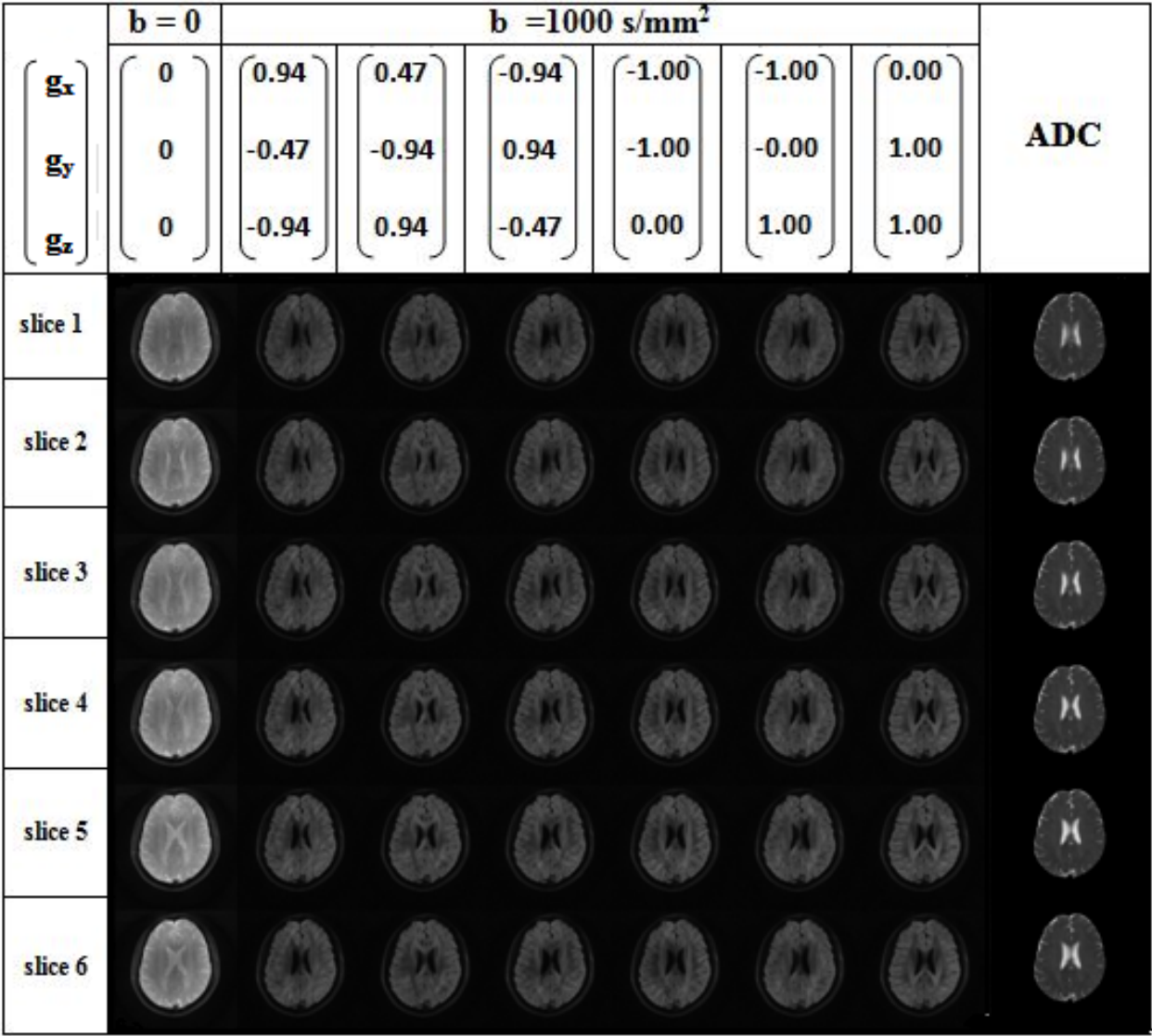
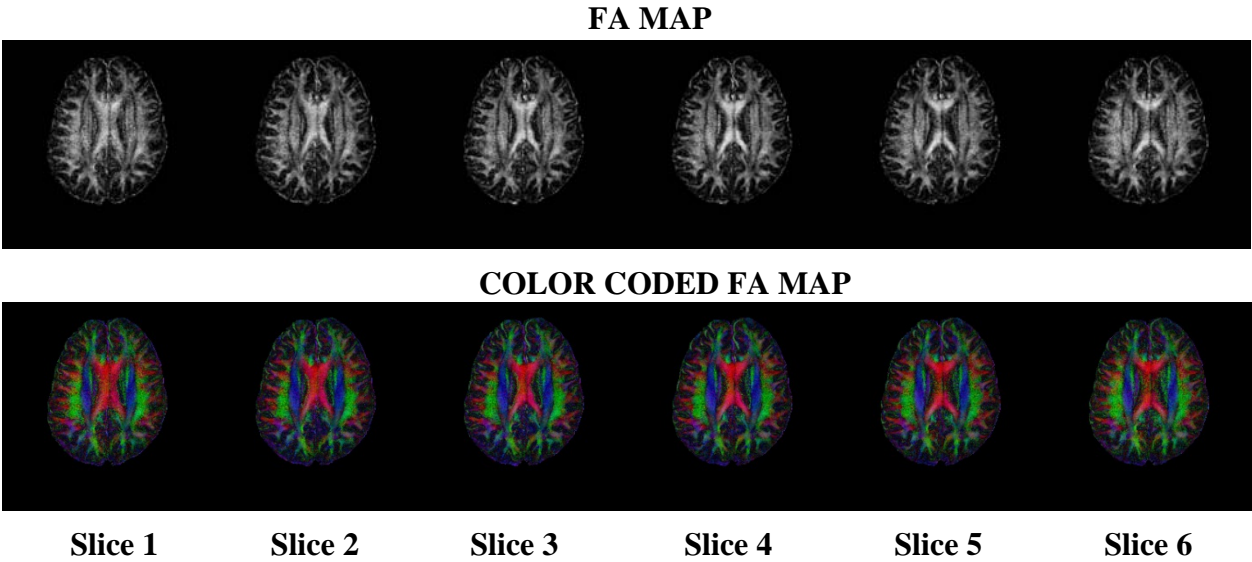


Figure 6



**Rapid Data Acquisition for PROPELLER-MRI:
A Combination of Iterative Reconstruction and Under-Sampling**

**Ashish A Tamhane¹, Konstantinos Arfanakis², Mark Anastasio³,
Xiadong Guo¹, Michael Vannier¹, Jia-Hong Gao¹**

¹Brain Research Imaging Center and Department of Radiology,
The University of Chicago, Chicago, IL

²Department of Biomedical Engineering, Illinois Institute of Technology, Chicago, IL

³Department of Biomedical Engineering, Washington University, Saint Louis, MO

Corresponding Author:

Jia-Hong Gao, Ph.D.

Brain Research Imaging Center

The University of Chicago

5841 South Maryland, MC 2026

Chicago, IL 60637

Tel: 773-834-0480

Fax: 773-834-7610

E-mail: jgao@uchicago.edu

Manuscript word count: 2916

Running head: Iterative Image Reconstruction using NUFFT for Undersampled
PROPELLER

ABSTRACT

PROPELLER (Periodically Rotated Overlapping parallel Lines with Enhanced Reconstruction) MRI is able to reduce motion and field inhomogeneity-related artifacts at the cost of longer scan time. Previous efforts by combining under-sampled PROPELLER acquisition and gridding reconstruction can reduce the acquisition time, however, this practice produced significant ghosting image artifacts or uneven smoothing across image space. To eliminate these imaging problems, an iterative reconstruction technique based on the non-uniform fast Fourier transform was developed to replace gridding reconstruction, and our experimental results demonstrated significant improvement in the imaging quality.

Keywords: PROPELLER, Undersampling, Iterative reconstruction

INTRODUCTION

PROPELLER¹ (Periodically Rotated Overlapping parallel Lines with Enhanced Reconstruction)-MRI has attracted a great attention of the MR community due to its significantly reduced sensitivity to motion related artifacts when compared with conventional Cartesian based multiple-shot turbo spin echo (TSE) acquisition. In PROPELLER, a set of parallel lines passing through the center of k-space is acquired in one TR, referred as a blade, which is then rotated around its center to cover the entire k-space (Fig 1 a). The central region of k-space(sampled by each blade) is used to correct rigid body motion between blades. However, redundant sampling near the center of k-space prolonged acquisition time for PROPELLER by at least 1.5 times when compared with its Cartesian based TSE. Hence, it is beneficial and necessary to reduce imaging time of PROPELLER acquisition to improve its clinical applicability.

In PROPELLER-MRI, significant reduction in acquisition time can be achieved by decreasing number of blades in sampling pattern. Under-sampling technique of acquiring every alternative blade proposed by Arfanakis² *et al* reduced imaging time by 50% but suffered from streaking artifacts and blurring along the direction of missing blades. These problems were reduced by He³ *et al*, when images were obtained by regularized iterative reconstruction instead of conventional gridding⁴. However, blurring along direction of missing blades could not be completely eliminated with iterative reconstruction.

In this study, a novel under-sampling strategy for PROPELLER trajectory was proposed to eliminate issues of blurring and streaking artifacts. A reduction in imaging time for PROPELLER trajectory was achieved by increasing width of each blade by under-sampling along phase encoding direction and reducing number of blades to cover entire k-space. If reconstructed using gridding, images from such under-sampled PROPELLER acquisition exhibited significant aliasing artifacts. It was demonstrated that use of regularized iterative image reconstruction could significantly reduce these aliasing artifacts. Also, motion estimation method has been modified for proposed under-sampled PROPELLER acquisition to improve accuracy of motion correction. Hence, it was demonstrated that a combination of iterative reconstruction and proposed under-sampling pattern reduces imaging time by 50 % and produced images with negligible aliasing artifacts while retaining advantages of motion correction when compared with sufficiently sampled PROPELLER acquisition.

METHODS

Sampling Strategy: In PROPELLER-MRI, k-space data for each blade are sampled at least with Nyquist rate such that the maximum distance between two adjacent points in frequency and phase encoding direction is $1/\text{Field of View (FOV)}$. Width of can be denoted as $L \cdot (1/\text{FOV})$, where L is number lines per blade. Assuming circular k-space coverage and FOV equal to 1 unit, total number of blades required to cover the entire k-space in sufficiently sampled PROPELLER acquisition is determined by,

$$B = (\Pi * P) / (2 * L) \quad (1)$$

Where P and B are number points per line and number of blades per acquisition, respectively. If each blade in an acquisition is under-sampled in phase encoding direction by *Undersampling_Factor*, then width of blade is changed to $(L * \text{Undersampling_Factor})$ and number of blades required is determined by

$$B = (\Pi * P) / (2 * L * \text{Undersampling_Factor}) \quad (2)$$

Undersampling_Factor is equal to one sufficiently sampled acquisition and in this study an acquisition with *Undersampling Factor* of two is considered. Hence, with *Undersampling Factor* equal to two, total number of blades required to cover the entire k-space are reduced by factor of two. As demonstrated in Figure 1, in sufficiently sampled acquisition, if there are 20 lines per blade then 10 blades are required to cover entire k-space (Figure 1a). However, if distance between adjacent lines is increased by factor of 2 then only 5 blades are required to sample the k-space (Figure 1b). With this sampling strategy, a significant improvement in imaging time can be achieved compared with sufficiently sampled acquisition. Two sampling patterns with 18 and 9 blades were used in this study and will be referred as S1 and S2 respectively in this study. S1 and S2 has under-sampling factor equal to 1 (Sufficiently sampled) and 2, respectively. Both sampling patterns contained 20 k-space lines per blade and 240 k-space samples per line. However, images exhibited significant aliasing artifacts if they were reconstructed using gridding algorithm.

Pre-reconstruction Data Processing: Before image reconstruction data were processed through phase correction, in-plane motion correction^{1,7} and correlation weighting¹ stages as shown in Figure 1c. Phase correction for each blade was performed by completely

removing phase of image space data for each blade. While estimating in-plane motion and computing correlation, central region of each blade are gridded on polar and/or Cartesian grids. The detailed procedure to estimate motion and correlation has been explained in reference¹. If each blade is under-sampled along phase encoding direction, gridded data from central region of each blade will exhibit Nyquist holes, which could adversely affect estimation of motion between blades. If wider convolution kernel used for this gridding procedure, then error because of Nyquist holes could be minimized. Hence, in this study, during motion correction and correlation weighting procedure, data from central region of each blade are gridded on Cartesian grid using convolution kernels (Kaiser- Bessel) of width 2/FOV and 4/FOV radius.

Image Reconstruction: Image reconstruction was performed separately by gridding and also with regularized iterative reconstruction as described below

1. Conventional PROPELLER image reconstruction: Gridding

In conventional PROPELLER image reconstruction, the non-uniform k-space samples are then gridded onto a Cartesian grid, and a 2D inverse fast Fourier transform (FFT) is applied on the Cartesian k-space data. Gridding is completed using:

$$M_c = \{[(M_p \bullet W) \otimes C] \bullet III\} \otimes^{-1} C \quad (3)$$

where M_c is the k-space data in a Cartesian grid, M_p is the data in the PROPELLER grid, W is the weighting function that compensates for the non-uniform sampling density, C is the convolution function, III is the Cartesian grid, \otimes and \otimes^{-1} represent the convolution and deconvolution operations, respectively. The weighting function, W , is non-zero only

at the sampling locations of the PROPELLER grid, and is estimated iteratively⁸. The convolution function, C , is also estimated iteratively⁸.

For gridding, a pre-sampled Kaiser-Bessel function with 300 samples within a width= $[5/(FOV)]$ and radius of $2/FOV$ was used as the convolution kernel. Linear interpolation was used to estimate values of the Kaiser-Bessel function corresponding to different distances between k-space samples in the PROPELLER and Cartesian grids. Deconvolution was performed in image space by dividing the reconstructed image by the inverse Fourier transform of the convolution kernel. All images were reconstructed into 512x512 matrices.

2. Iterative image reconstruction for PROPELLER MRI using NUFFT

Images reconstructed using gridding from under-sampled PROPELLER acquisition show significant aliasing artifacts. In this study, iterative reconstruction method introduced in reference⁶ was applied to data from under-sampled PROPELLER acquisitions to reduce these artifacts. The goal of the iterative image reconstruction is to reconstruct discrete image x of an object on Cartesian grid from the noisy k-space samples M_p . In this work, the estimate of the object on a Cartesian grid was obtained by minimizing a penalized weighted least squares cost function:

$$\psi(x) = \frac{1}{2} \|M_p - Ax\|_w^2 + \beta R(x) , \quad (4)$$

where $R(x)$ is a quadratic penalty function and β is a penalty value that controls the influence of $R(x)$ on the cost function. This method will be referred as Quadratic Penalized Weighted Least Squares (QPWLS) in this study. The operator A maps the

estimate of the object residing on a Cartesian grid x to k-space samples on the PROPELLER grid and performed using NUFFT. W is the weighting function that compensates for the non-uniform sampling density. In PROPELLER, W does not only contain information about k-space sampling density but also about correlation weighting between each blade. Hence, an iterative reconstruction was solved by minimizing weighted least square cost function instead of least squares approach. The cost function in Equation (4) was minimized using the conjugate gradient (CG) method with the Fletcher-Reeves update formula. All images were reconstructed into 512x512 matrices.

Numerical Simulations: PROPELLER k-space data were simulated using the Shepp-Logan phantom⁹. The k-space representation of the Shepp-Logan phantom is known analytically. Therefore, it was possible to accurately simulate sampling with any pattern. Convergence of QPWLS for sufficiently sampled PROPELLER acquisition has been analyzed previously⁶. Similarly, convergence of the QPWLS reconstruction for under-sampled acquisition was assessed by plotting Root Mean Square (RMS) error versus number of iterations in reconstruction. The RMS error was calculated as follows from noise-free Shepp-Logan phantom data

$$\text{RMS} = \sqrt{\frac{\sum_{i=1}^N (f_i - f_{ni})^2}{N}} \quad (5)$$

where f_n is the image produced in the n^{th} iteration, f is the true object, i is the index number of a voxel, and N is the number of voxels in each image. The number of iterations for which the algorithm appeared to converge was determined. Same procedure was repeated for different penalty values (0.02, 1). The mean zero noise of standard

deviation of 0.01 was added to real and imaginary part of k-space and images were reconstructed using gridding reconstruction and QPWLS.

Experiments on Phantom and Humans: Scans were performed on a physical phantom and the brain of four healthy human subjects using a 3T Philips MRI scanner (Philips, Best, The Netherlands) at University of Chicago and the standard Philips 8 channel standard head coil. Informed consent was obtained from the human volunteers. PROPELLER sequence was implemented on scanner and data were acquired with this sequence and the following imaging parameters: TR=4000 ms, Echo Train Length (ETL)=20, field of view of 24 cm x 24 cm, slice thickness of 3 mm, and the sampling patterns mentioned above. For 6 slices, imaging times for S1 and S2 are 72 and 36 seconds, respectively. Images for each channel were reconstructed separately and then combined with sum of squares approach. Regions of interest (ROIs) were selected in areas of the phantom and the brain with relatively uniform signal intensity, and the SNR over each ROI was estimated by dividing mean signal by standard deviation of signal from that region.

Finally, motion correction was tested with under-sampled PROPELLER data. Two sets of data were acquired as follows 1) without subject motion 2) with subject motion. During data acquisition with motion, subject was asked to move head freely between each TR. This procedure created jerk motion between blades rather than continuous motion. As described previously, motion estimation process was performed using two convolution kernels, one with radius of $2/\text{FOV}$ and other with $4/\text{FOV}$. Image quality was

assessed visually for motion correction by independent observers.

RESULTS

Figure 2 (a) shows ideal Shepp-Logan phantom and image reconstructed using gridding (b) and QPWLS (c) for sampling pattern S2. Noise was not added to simulated k-space. Image reconstructed using gridding suffers from ghosting artifacts but image reconstructed using QPWLS does not exhibit such artifacts. Figure 2 (d) shows plots of a line passing through center of FOV of images in figure 2 (a, b, c). Profile for QPWLS image is very close to ideal Shepp-Logan phantom when compared with profile of image obtained by gridding.

Figure 3 shows the graph of mean RMS error against number of iterations for QPWLS. Mean RMS remained constant after 10 iterations for multiple penalty values and QPWLS was terminated after 20 iterations. This conservative termination criterion was selected because image reconstruction time was not considered as a constraint in this study.

Figure 4 (a, b, c) shows images of Shepp-Logan phantom, phantom and human brain acquired with sufficiently sampled acquisition and reconstructed using gridding. Figure 4 (d, e, f) shows images of same slices for Shepp-Logan phantom, phantom and human brain acquired with under-sampled acquisition and reconstructed using gridding. If images were reconstructed using QPWLS (penalty=0.02) then image artifacts caused because of under-sampling were minimized (Figure 4 g, h, i). With increase in penalty

value, resolution in QPWLS decreased and SNR increased⁶. For comparing in-plane resolution, a resolution pattern was magnified from physical phantom (Figure 4 b, e, i).

Finally, motion correction in under-sampling was demonstrated in presence and absence of in-plane motion. In figure 5, images (a, c, e) correspond to data, when subject was asked to avoid any motion, while images (b, d, f) correspond to data when subject was asked to move head freely, during acquisition. Figure 5 (a, b) shows images without any motion correction. Figure 5 (c, d) and (e, f), shows images after motion correction using kernel of radius $2/\text{FOV}$ and $4/\text{FOV}$, respectively.

DISCUSSION

Results from (Figure 3 and 4) demonstrate that, for under-sampled PROPELLER acquisition gridding reconstruction produces images with significant aliasing artifacts. Data from each blade produce aliasing artifacts along phase encoding direction. But phase encoding direction is rotated along each blade. This results in complicated aliasing pattern in final reconstructed image as shown in Figure 3. However, QPWLS reconstruction reduced these aliasing artifacts by penalizing irregularities in neighboring voxels and minimizing l_2 norm. Images are reconstructed with QPWLS shows significant reduction of artifacts when compared with gridding. Hence a combination of under-sampled PROPELLER and QPWLS can be used to save 50% of imaging time. Similar observations were made for all human subjects. The cost of savings in imaging time has to be paid in terms of reduction in SNR for under-sampled acquisition. Approximately,

50% reduction in SNR was observed for all four subjects in region of frontal lobe white matter.

In this study, weighted least squares approach was preferred since, in PROPELLER sampling density compensation function also contains information about correlation weighting. Correlation weighting is used to exclude or punish data from blades corrupted by through plane motion.

Also, quadratic penalty function was used in iterative reconstruction (QPWLS). For QPWLS, increase in penalty value, reduces resolution and increases smoothness and SNR in image⁶. To preserve resolution, a small penalty value equal to 0.02 was chosen in this study. For this penalty value, a comparable resolution was obtained as in case of images obtained by sufficiently sampled PROPELLER using gridding reconstruction (Figure 4). Alternatively, total variation (TV) penalty function technique has been incorporated in iterative reconstruction in place of quadratic penalty function and similar results were observed. However, further research is required to quantify image quality different regularization functions.

It has been suggested a PROPELLER under-sampling trajectory, which excluded every alternative blade is efficient way to reduce imaging time². However, this under-sampling scheme has caused blurring or smoothing and streaking along the direction of missing blades. HE³ *et al* have combined regularized iterative reconstruction with alternative blade missing acquisition. Iterative reconstruction was able reduce out some significant

streaking artifacts but cannot recover high-resolution information left out in acquisition. These artifacts and smoothing increased as gap between blades increases. Also, problem of uneven smoothing across image space may worsen in presence of significant subject motion. In PROPELLER, motion correction is divided into rotation and translation correction and rotation correction is performed by rearranging angles between blades for compensating rotation between individual blade and the reference blade. In case of significant motion between blades for alternative blades missing trajectory, rotation correction can further widen the gap between adjacent blades and may increase blurring and streaking artifacts. Proposed under-sampling scheme reduced this possibility because no gap was left between blades.

In presence of significant in-plane motion, motion correction was performed on data from proposed under-sampled acquisition and improvement in image quality was observed. For rotation and translation estimation, data from each blade of central region of k-space are gridded on polar and Cartesian grid respectively. In case of sufficiently sampled case, convolution kernel of radius equal to $2/\text{FOV}$ was sufficient for this process since, maximum distance between two adjacent points in one blade is $1/\text{FOV}$. But for under-sampled acquisition proposed in this study, gridding procedure with this size of convolution kernel creates Nyquist holes in gridded data, which affects estimation of rotations and translations (Figure c, d). Hence, wider kernel of radius equal to $4/\text{FOV}$ was used and improvement in motion correction was observed. Robustness of motion correction was demonstrated by performing motion correction on data collected with and without motion. In both cases, when kernel of radius $4/\text{FOV}$ was used for motion

estimation, superior image quality was observed and more details in image were visible. Similarly, to compute correlation weighting between blades, data from central region of blades are gridded before computing correlation between them. A use of wider kernel reduced effect of under-sampling on these computations.

This technique was demonstrated for TSE based sequence. PROPELLER acquisition can also be accelerated using its GRASE and EPI based successors named TurboProp and PROPELLER-EPI. In principle, proposed technique can be extended to these variants of PROPELLER acquisition.

Alternatively, reduction in imaging by increase in width of blade and decrease in number of blades can also be achieved with a parallel imaging technique, such as Generalized Autocalibrating Partially Parallel acquisitions (GRAPPA)¹²⁻¹⁴. However, this method requires acquisition of calibration data for purpose of reconstruction, which increases imaging time. The subject motion between calibration data and accelerated data could cause significant degradation of image quality. Also, calibration data could be embedded in each blade but could increase imaging time significantly and reduce effective acceleration factor. Skare¹⁶ *et al* used a pair of orthogonal blades for a purpose of auto-calibration but these two blades are needed to be aligned before calibration. This method can be sensitive to motion between these two blades. Recently, Li¹⁷ *et al* proposed split blade technique for auto-calibration. This method reduced imaging time significantly but because of split blade method effective width of each blade was reduced when compared

with proposed method and thin blades are not ideal for estimating rotations between blades

In conclusion, very effective method for reducing PROPELLER imaging time was introduced in this study without compromising any of its advantages such as motion correction. This technique can help to reduce imaging time of PROPELLER by 50% or can increase number of slices can be acquired in same imaging time by factor of two.

REFERENCE

1. Pipe JG. Motion correction with PROPELLER MRI: Application to head motion and free-breathing cardiac imaging. *Magn Reson Med* 1999;42:963–969.
2. Arfanakis K, Tamhane AA, Pipe JG, Anastasio MA. K-space undersampling in PROPELLER imaging. *Magn Reson Med* 2005;53:675-683.
3. He Q, Weng D, Zhou X, Ni C. Regularized Iterative Reconstruction for Undersampled BLADE and Its Applications in Three-point Dixon Water–fat Separation. *Magn Reson Med* 2011; (In-press).
4. Jackson JJ, Meyer CH, Nishimura DG, Macovski A. Selection of a convolution function for Fourier inversion using gridding. *IEEE Trans Med Imaging* 1991;3:473-478.
5. Fessler JA, Sutton BP. Nonuniform fast Fourier Transform using Min-Max interpolation. *IEEE Trans Signal Proc* 2003;51:560-573.
6. Tamhane AA, Anastasio MA, Gui M, Arfanakis K. Iterative Image Reconstruction for PROPELLER MRI Using the Nonuniform Fast Fourier Transform. *J Magn Reson Imag* 2010;32; 211-217.
7. Tamhane AA, Arfanakis K. Motion correction in Periodically Rotated Overlapping Parallel Lines with Enhanced Reconstruction (PROPELLER) and TurboProp MRI. *Magn Reson Med* 2009;62; 174-182.
8. Pipe JG, Menon P. Sampling Density Compensation In MRI: Rationale and an

Iterative Numerical Solution. Magn Reson Med 1999;41; 179-186.

9. Shepp LA, Logan BF. The Fourier reconstruction of a head section. IEEE Trans Nucl Sci 1974;NS-21:21– 43.
10. Pipe JG, Zwart N. Turboprop: Improved PROPELLER imaging. Magn Reson Med 2006;55:380-385.
11. Wang FN, Huang TY, Lin FH, Chuang TC, Chen NK, Chung HW, Chen CY, Kwong KK. PROPELLER EPI: an MRI technique suitable for diffusion tensor imaging at high field strength with reduced geometric distortions. Magn Reson Med 2005;54:1232-1240.
12. Griswold MA, Jakob PM, Keidemann RM, Nittka M, Jellus V, Wang J, Kiefer B, Kaase A. Generalized autocalibrating partially parallel acquisitions (GRAPPA). Magn Reson Med 2002;47:1202–1210.
13. Beatty PJ, Brau AC. Parallel imaging PROPELLER with across-blade autocalibration. In Proceedings of the Workshop on non-cartesian MR of ISMRM, Sedona, Arizona, USA, 2007.
14. Blaimer M, Barkauskas K, Kannengiesser S, Breuer F, Jakob PM, Duerk JL, Griswold MA. Artifact reduction in undersampled BLADE/PROPELLER MRI by k-space extrapolation using parallel imaging. In Proceedings of the 14th Annual Meeting of ISMRM, Seattle, Washington, USA, 2006. p 5.
15. Chuang TC, Huang TY, Lin FH, Wang FN, Juan CJ, Chung HW, Chen CY, Kwong KK. PROPELLER-EPI parallel imaging using a circularly symmetric phased-array RF coil at 3.0 T: application to high-resolution diffusion tensor imaging. Magn Reson Med 2006;56:1352–1358.
16. Skare S, Newbould RD, Nordell A, Holdsworth SJ, Bammer R. An auto-calibrated angularly continuous, two-dimensional GRAPPA kernel for Propeller Trajectories. Magn Reson Med 2008;60:1457–1465.
17. Li Z, Pipe JG, Aboussouan E, Karis JP, Huo D. A Parallel Imaging Technique Using Mutual Calibration for Split-Blade Diffusion-Weighted PROPELLER. Magn Reson Med 2011;65:638–644.

Figure 1: (a) sufficiently sampled PROPELLER sampling with distance between adjacent points in one blade is equal to $1/\text{FOV}$. (b) Undersampled PROPELLER sampling in which, distance between two lines in one blade was doubled ($2/\text{FOV}$). As a result width of blade increased and number of blades required to cover entire k-space and imaging time was halved (c) work flow for under-sampled PROPELLER acquisition and image reconstruction

Figure 2: (a) shows ideal Shepp-Logan phantom, (b, c) are images reconstructed from simulated k-space data with under-sampled PROPELLER acquisition with under-sampling factor equal to 2. Image (b) was reconstructed using gridding while (c) was reconstructed using QPWLS. No noise was added to k-space. Plot (d) denotes profiles of lines passing through three images.

Figure 3: RMS error plot for QPWLS with penalty = 0.02 and 1 against number of iterations. RMS error remained constant after 10 iterations. Hence during all following experiments, iterations for QPWLS are terminated after 20 iterations.

Figure 4: Images of (a, d, g) Shepp-Logan phantom (numerical simulations), (b, e, h) phantom and (c, f, i) human brain. Images (a, b, c) are reconstructed using gridding from data acquired with sufficiently sampled PROPELLER acquisition. Images (d, e, f) and (g, h, i) are reconstructed from under-sampled PROPELLER data using gridding and QPWLS, respectively.

Figure 5: Motion correction with PROPELLER under-sampling. Figure (a, c, e) and (b, d, f) are images from acquisition without and with subject motion. Images (c, d) are corrected for motion using interpolation kernel of radius $2/\text{FOV}$, while images (e, f) are corrected for motion using interpolation kernel of radius $4/\text{FOV}$.

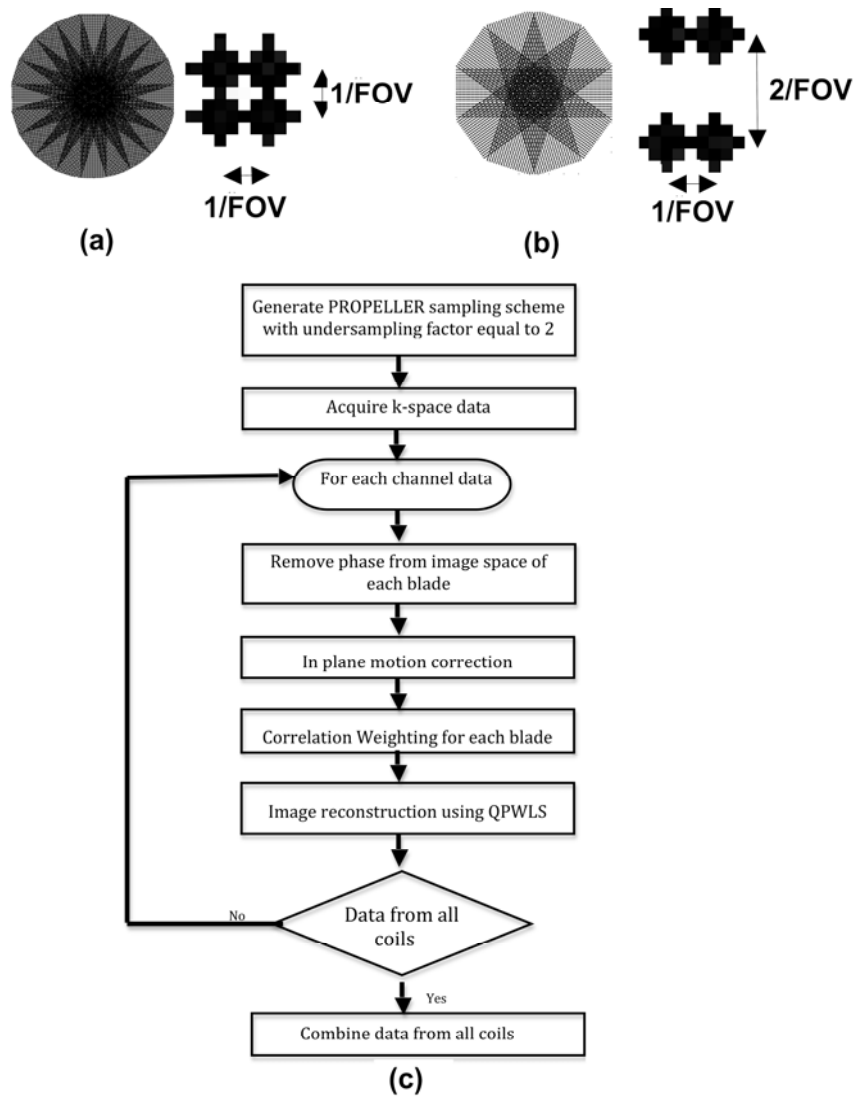


Figure 1

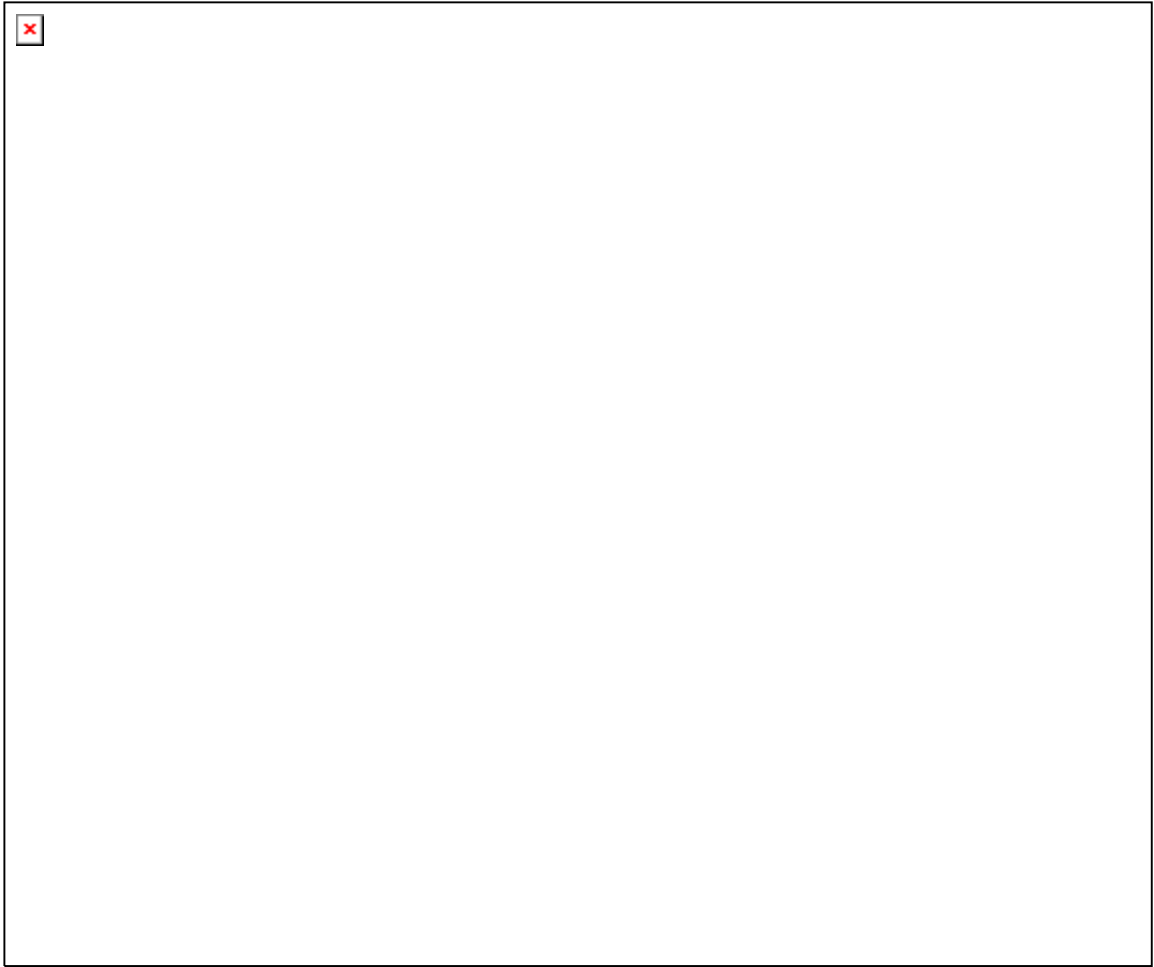


Figure 2

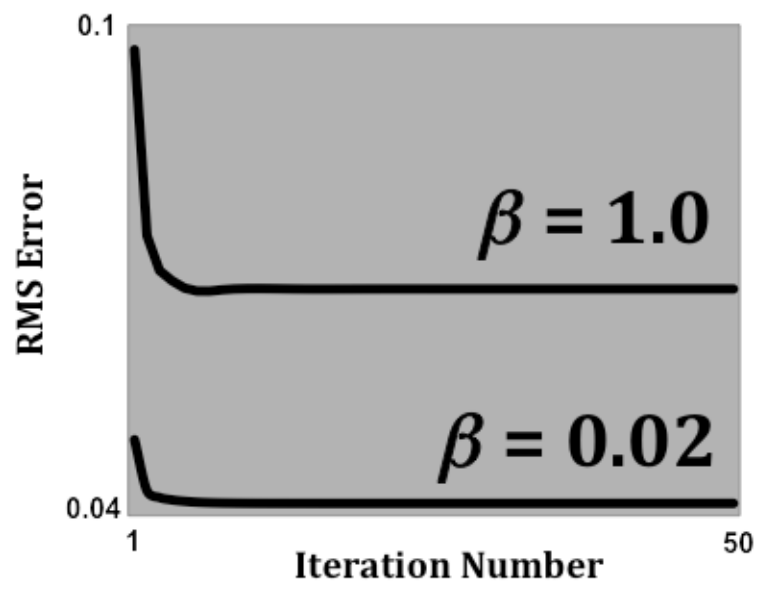


Figure 3

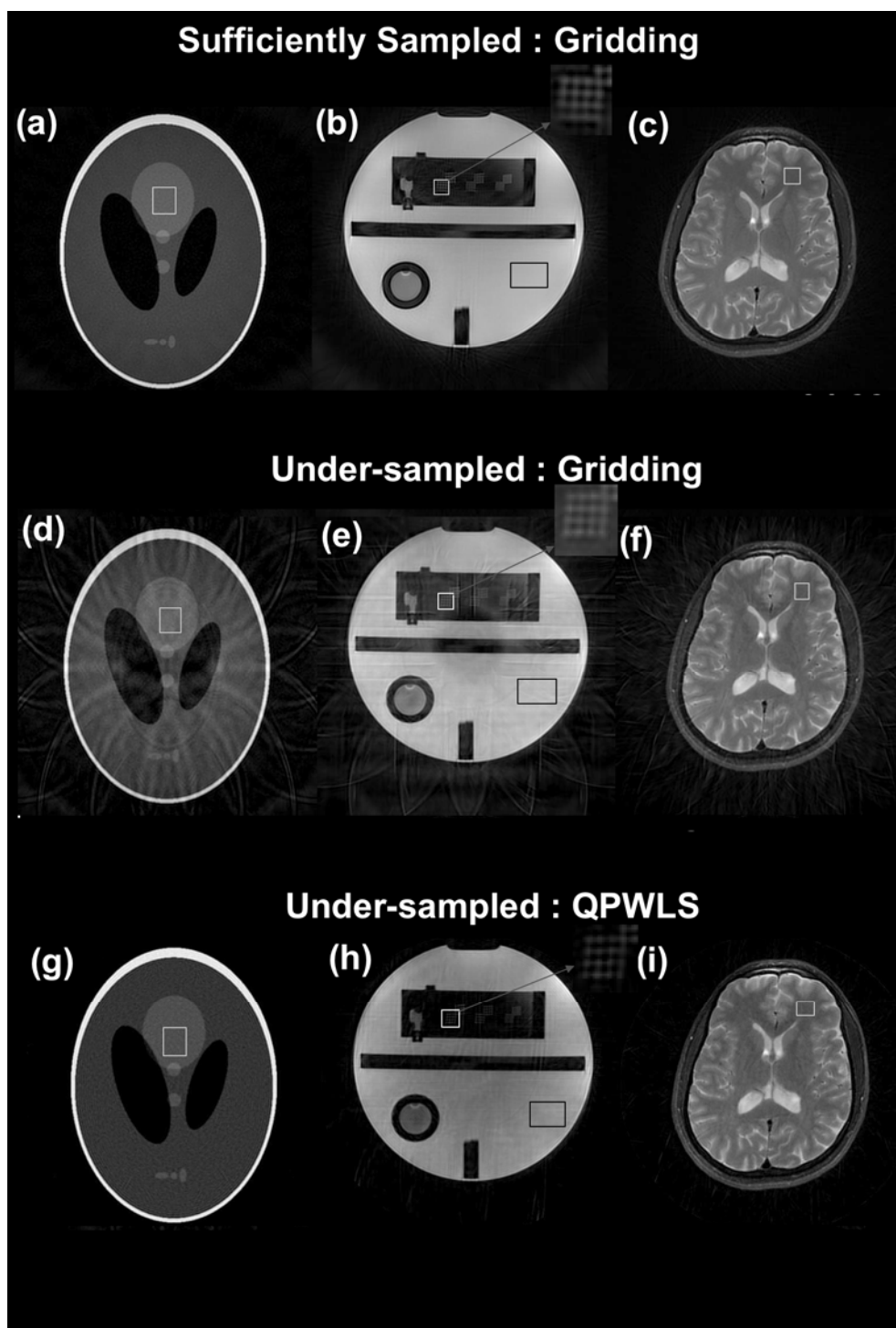


Figure 4

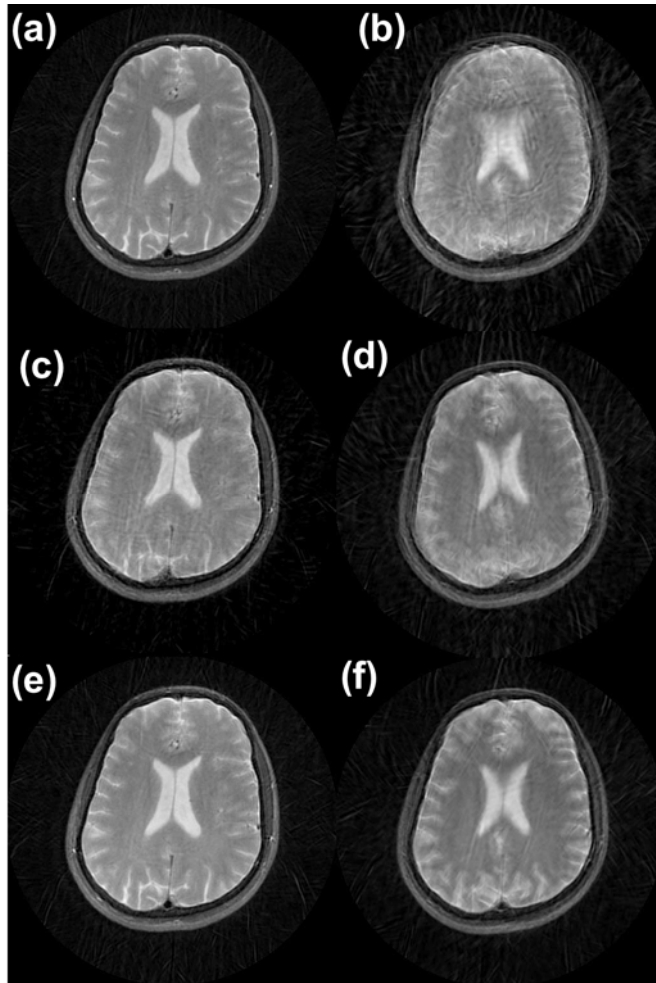
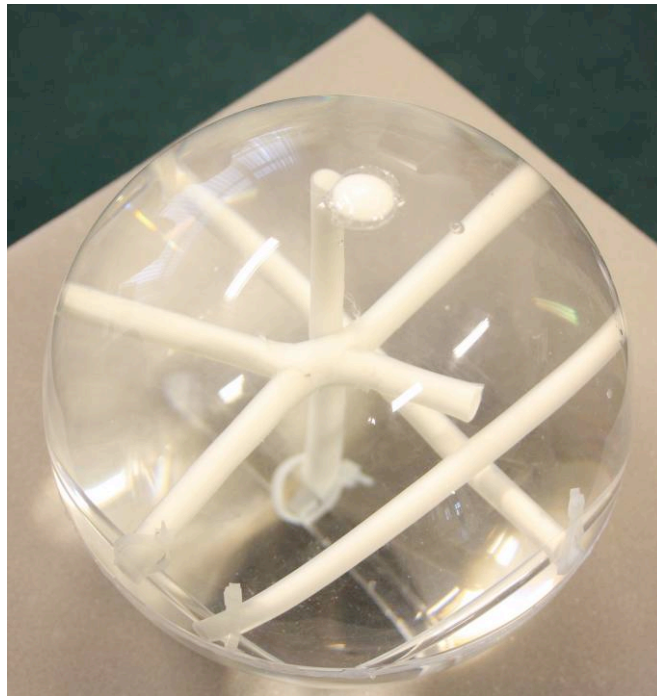


Figure 5

ANISOTROPIC PHANTOM

FOR DIFFUSION WEIGHTED MRI APPLICATIONS



Instruction Manual

Pim Pullens and Claudia Goebel

© 2010, Brain Innovation bv, Maastricht, The Netherlands

1 Product Classification and Purpose

The anisotropic PHANTOM is a synthetic physical auxiliary device for diffusion weighted (DW) magnetic resonance imaging (MRI) studies.

Diffusion tensor-based fiber tracking is limited in resolving complex white matter of cytoarchitecture, such as diverging or crossing nerve fibers. [1] Fiber properties, measurement parameters, and resulting data quality as well as reconstruction algorithms determine the visualization of fiber bundles, not only its precision or accuracy but also its reproducibility.

Hardware phantoms have the advantage of a controllable standard going beyond computer simulations. They can be also subject to simulation studies.

In comparison to reference [1] this Anisotropic Phantom contains both 3 straight, nearly orthogonal phantoms and 1 crossing phantom. Its structural design, the polyester fiber material arranged in a particular way in tubes, the isotropic, and aniso-

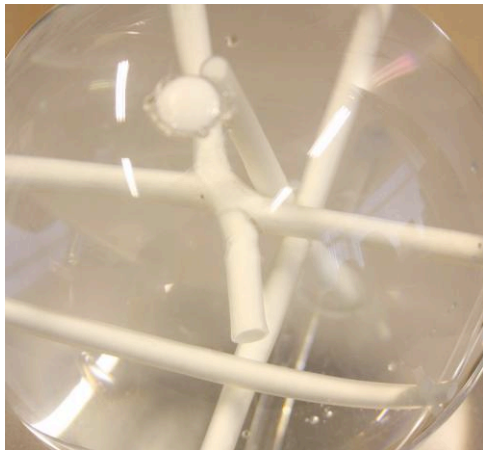


Fig 2 Straight and crossing phantoms

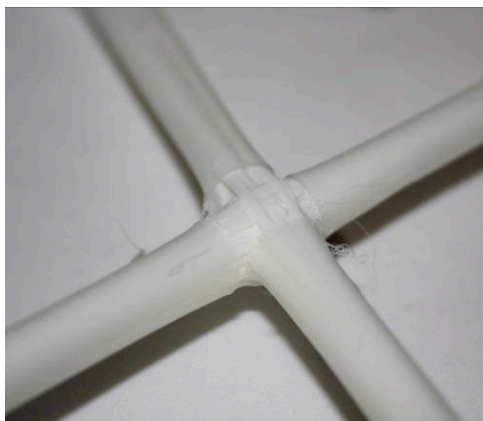


Fig 3 Crossing polyester fibers in the tube

tropic properties of included water allow the evaluation of data acquisition conditions you might look for *quality control* measures or *calibration* of DW-MRI sequences, DW-MRI *sequence development*, *multi-center DW-MRI studies comparability tests* as well as for studying new data analysis and visualization algorithms to tackle fiber tractography problems.

This auxiliary device has no measurement function itself. Within the tolerances of manufacturing process, or the uniformity of the test probes, it is possible to control the factors affecting anisotropic water diffusion.

The Phantom can be used in combination with the BrainVoyager QX software for analysis and visualizations of DW images. This software is not part of this device and contract but can be purchased at Brain Innovation. The Phantom can also be used with other imaging software packages.

The Phantom cannot be declared as “Medical Product” for diagnostic and therapy of humans and shall not be used indirectly for this purpose. Due to its model character it is for research and academic applications only. It is not suitable for simultaneous measurements with humans or animals in the MR scanner.

Limited Purpose and Knowledge Transfer.

According to Hubbard and Parker [2] “... the design of (such a) phantom is inevitably an approximation to brain tissue, which means that significant uncertainty remains in the extrapolation of our understanding of the diffusion signal obtained from the physical phantoms to the *in vivo* experiment.” Synthetic fiber phantoms are powerful to provide evidence of the performance of a diffusion MRI measurement and/or of a given tracking algorithm in a controlled environment. “However, the dissimilarity between the microscopic geometry and permeability characteristics of the phantoms and that of brain tissue sets a limit on the degree of validation that they can provide.”

2 Phantom Design and Test Measurement

2.1 Phantom Construction and Material

The Phantom contains of 3 tubular anisotropic diffusion phantoms and 1 crossing phantom. The 3 straight tubular phantoms are arranged in nearly orthogonal directions (see Figures 2 and 3). The small angles of the crossing phantom are roughly 60 degrees each.

The tubular phantoms are 135-140 mm long, and the diameter is 6.5-7.5 mm.

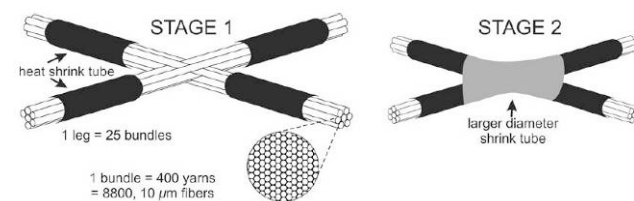


Figure 4 Scheme of Phantom tube construction with crossing yarn fiber bundles inside

Each tube contains 10.000 (-2) parallel polyester yarns (KUAG Diolen, 22 dtex 18). Fibers are solid (not hollow), thus the phantom is a *model for extra-cellular restricted diffusion*. Each yarn is made up of 18 fibers, so each tubular phantom contains 180.000 (-36) fibers.

One leg of the crossing phantoms contains $25 * 400 \text{ yarns} * 18 \text{ fibers} = 180.000$ (-36) fibers.

The yarns are constrained by a color-less polyolefin shrink tube (Farnell inOne, NL).

The 4 phantoms are set up in a spherical 16 cm plastic sphere. The rods supporting the tubular phantoms are made from acrylate.

The phantom is filled with a solution of 0.03 g/l $\text{MnCl}_2 \cdot 4\text{H}_2\text{O}$ mimicking human white matter T_2 at 3 Tesla, 0.5 g/l NaN_3 and 4 g/l NaCl, for conservation and coil loading in de-mineralized (distilled) water.

A more detailed description of the Phantom production process and its properties can be found in reference [1].

All used material is of course MR compatible.

2.2 Test DTI measurement.

In our test we measure the apparent diffusion of the Phantom, calculate the mean diffusivity relative to a spatial unit = voxel, and the fractional anisotropy.

The Apparent or measured Diffusion Constant (ADC) shows the amount of diffusion. It is the *average* of all the microscopic displacements, which are present in a displayed voxel.

Mean Diffusivity (MD) is the mean diffusivity in a selected voxel.

Fractional Anisotropy (FA) demonstrates that in a selected voxel (measurement unit), there is a preferred diffusion direction.

Take care, low fractional anisotropy does not mean that there is no organization in that voxel.

Test measurement and data analysis

Scanning protocol

DW-MRI Data

- Siemens Allegra 3T, birdcage coil
- 12 directions + b0
- $b=1000 \text{ s/mm}^2$
- 75 slices
- 128 x 128 matrix, FOV 256 x 256 mm, resulting in 2 x 2 x 2 mm voxels
- TR/TE 10300/85 ms

Anatomy

- ADNI MPRAGE
- 192 slices
- FOV 256 x 256 mm
- 1 x 1 x 1 mm voxels

Data processing

The DTI DICOM data and MPRAGE DICOM data of the Phantom have been imported into BrainVoyager QX. The DTI data have been analyzed in the DTI module.

This is the standard protocol for DW-MRI data processing in BrainVoyagerQX. For more information, see the **DTI Getting Started Guide** available via <http://support.brainvoyager.com>

1. DMR creation from DW-MRI data
2. tensor calculation, FA and ADC maps on the DMR
3. VMR creation from MPRAGE data
4. co-registration of DMR to VMR
5. VDW creation
6. mask creation on VMR to eliminate background noise
7. tensor, FA, ADC calculation using mask
8. fiber tracking

Below you can see details of MD and FA maps in slice-space calculated and displayed in

BrainVoyager QX.

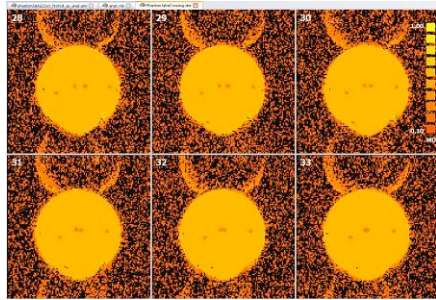


Fig 5 Phantom mean diffusivity (MD) map

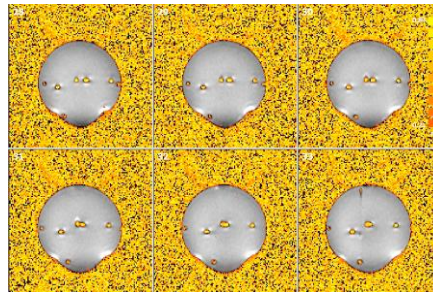


Fig 6 Phantom fractional anisotropy (FA) map

Below you can see details of MD and FA maps in volume-space in BrainVoyager QX. The data outside of the phantom are masked out.

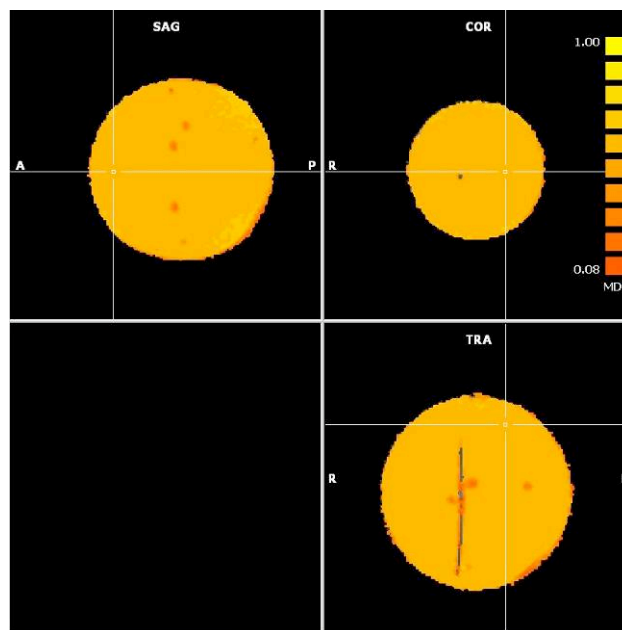


Figure 7 Phantom mean diffusivity (MD) map

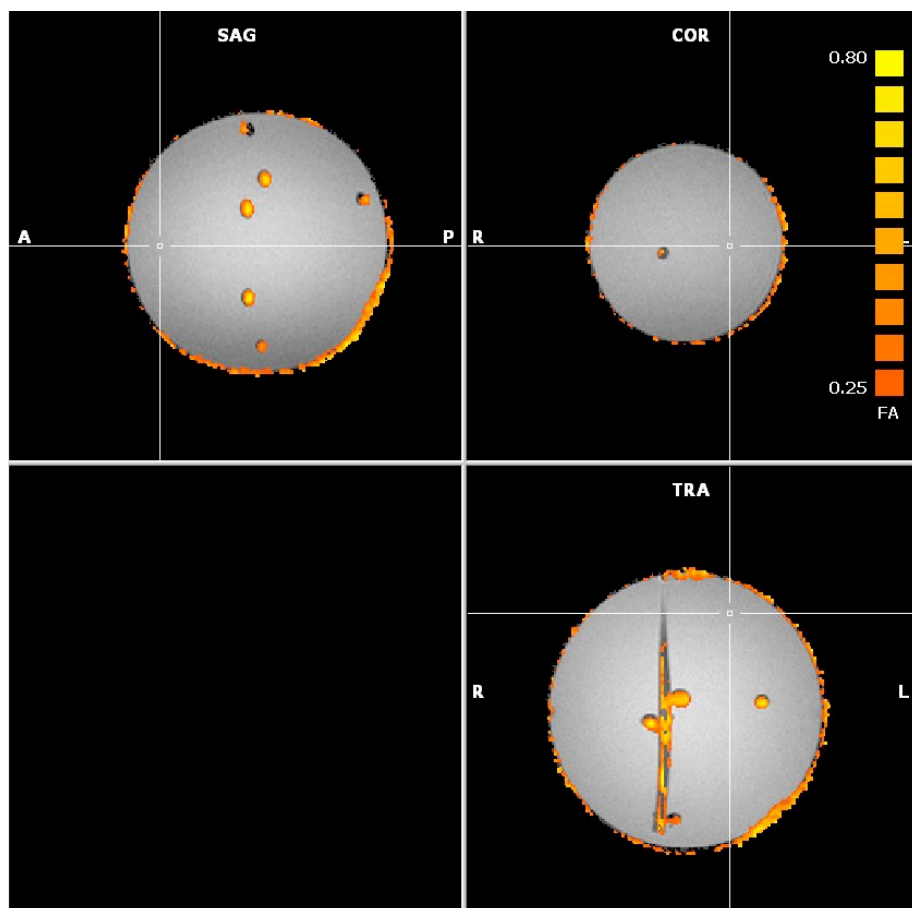


Figure 8: Phantom fractional anisotropy (FA) map.

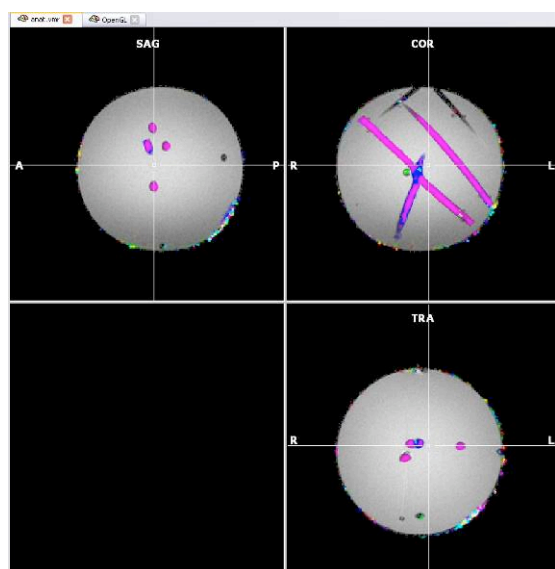


Fig. 9: Phantom color direction map of tensors in 3D volume space in BrainVoyager QX.

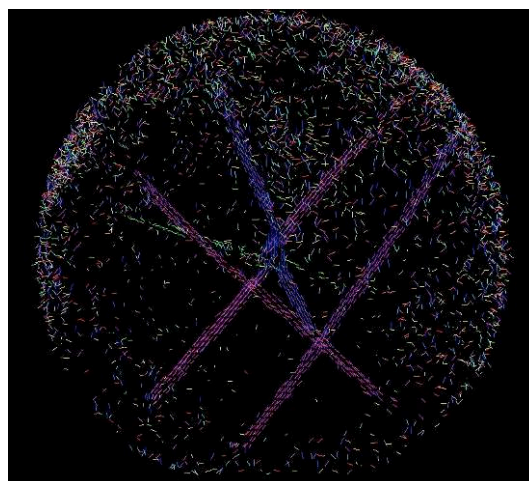


Fig. 10: Phantom 3D tensor display in the BrainVoyager QX Surface Module.

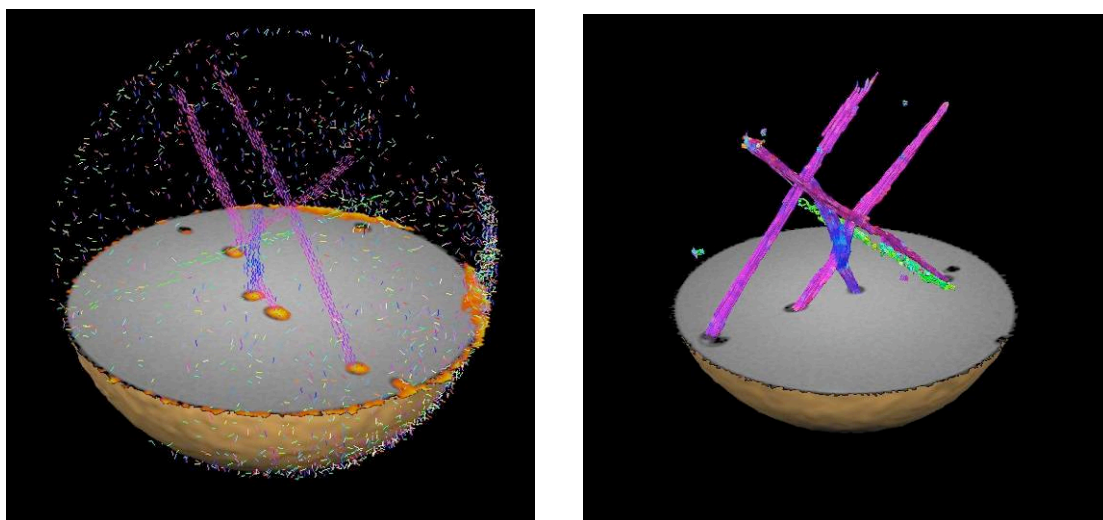
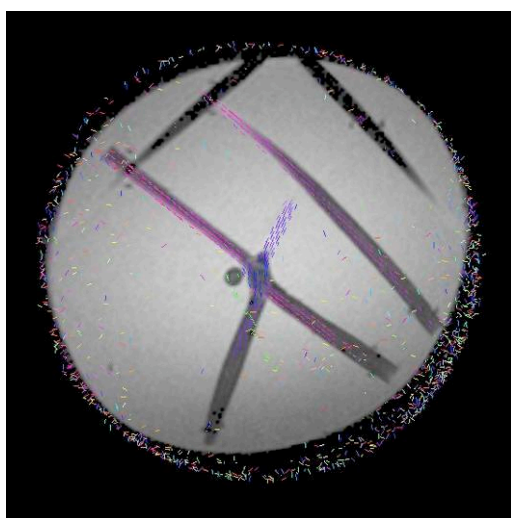


Figure 11: Phantom tensors and fiber tracks in BrainVoyager QX Surface Module.

Looking to the interrupted green fiber bundles of the right picture above, oriented in x-direction of the BrainVoyager QX Surface Module (equals y-direction of the Siemens Allegra scanner) you will notice that the tracking does not work so well in comparison to the y-direction fiber bundles (equals z-direction in Siemens system).



Here the crossing fibers were measured along the z-plane of the scanner and the fiber displays are better.

We observed ADC and FA values are not equal in the x, y and z oriented phantom tubes. According to our experience and with reference to the coordinate system of the Siemens MR scanner you receive the best ADC and FA values in z-direction and the worst ADC and FA values in y-direction, and in x-direction a quality of somehow in between.

You can explore those data.

Figure 12: Crossing phantom tensors in z-plane of BVQX SM.

These differences might be related to gradient miscalibration [4]. This effect was also observed in human white matter oriented parallel or perpendicular to the main magnetic field [5]. Here more research has to be done.

Remark: X, Y, Z direction naming might be different in other MR scanner systems. Check the vendor documentation.

3 Conditions of Use

3.1 General inspection. Setup suggestions

Brain Innovation cannot claim a general, scanner system independent, detailed, and precise instructions for a measurement or study involving the Phantom, since every MRI facility or MR scanner has its own properties and requirements. However, the physical properties of the phantom design shall not change except the measured diffusion anisotropy.

* Keep the environmental conditions (e.g. temperature) equal. The results obtained in [1] are valid for room temperature, therefore we recommend scanning at room temperature (18-23 deg. Celsius).

* Inspect the Phantom regularly before using it. Search for damage or leaks.

* Position the phantom in a holder suitable for spherical phantoms or on a bean bag.

* The tubular phantoms may be oriented in any direction, but a first measurement should start with the nearly orthogonal tubular phantoms oriented in the x (up-down), y (left – right direction) and z (direction of the bore) axes of the scanner. [Consider also our observations described on p 8].

* Evaluate also the crossing phantom in all 3 directions

3.2 Example MR protocol and procedure

First apply a localizer scan. Ensure that the phantom is in the center of the image and coil.

The next step is a diffusion-weighted scan. Use an isotropic voxel size and choose enough slices to cover the whole phantom. We advice to use a *b*-value of around 1000 s/mm², but other values may be used as well. Use at least 6 different diffusion directions + a *b*0 image to reconstruct the diffusion tensor and related measures such as mean diffusivity or fractional anisotropy.

Researchers who would like track fibers in *BrainVoyager QX* need a 3d T1 weighted structural MR scan (1*1*1 mm³) as reference for the DWI data reconstruction (suggested measurement direction - saggital slices).

4 Support

For further questions or customer support please write to support@brainvoyager.com.

Additional information may also be found at <http://www.brainvoyager.com/diffusionphantoms>

5 Safety Regulations/ WARNINGS

5.1 Temperature

Keep the phantom away from frost. Do not expose the phantom to extreme heat. It is recommended to store the phantom between 10 and 40 degrees Celsius.

5.2 Physical harm

To prevent damage to the phantom, do not puncture or drop and avoid contact with sharp objects. In the event the Phantom has a leaky gasket or broken sphere the item should not be used in the MR environment to avoid consequential damages of other equipment.

5.3 Chemical harm

The phantom contains a MRI solution, which is harmful to the environment and is dangerous when swallowed. Refer to chemical material safety sheets for disposal of the MRI solution. The solution is not for consumption.

This phantom is manufactured in The Netherlands.

According to Dutch safety regulations, no warning signs need to be attached to the phantom, since concentrations of dangerous chemicals are low.

For the sake of completeness we include the safety sheets for the chemicals in the phantom:

MnCl₂ · 4 H₂O

R 22: Harmful if swallowed.

R 48: Danger of serious damage to health by prolonged exposure.

R 52: Harmful to aquatic organisms.

NaCl

S 24: Avoid contact with skin.

S 25: Avoid contact with eyes.

NaN₃

R 28: Very toxic if swallowed.

R 32: Contact with acids liberates very toxic gas.

R 50: Very toxic to aquatic organisms.

R 53: May cause long-term adverse effects in the aquatic environment.

S 45: In case of accident or if you feel unwell, seek medical advice immediately (show the label where possible).

S 60: This material and its container must be disposed of as hazardous waste.

S 61: Avoid release to the environment. Refer to special instructions / Safety data sheets.

6 End User Agreement. Warranty Conditions.

This end user and warranty agreement is a contract between the Manufacturer Brain Innovation (BI), the Seller and the Buyer or End User of the Phantom, as individual or legal entity. It shall protect all professional parties.

Intellectual property - The Phantom design (except general design of fiber tubes) and especially the manufacturing process are original ideas of its developer - WLPM Pullens (Brain Innovation bv, Maastricht, The Netherlands) [1].

Copyright - WLPM Pullens and Brain Innovation bv, Universiteitssingel 40, 6229 ER Maastricht, The Netherlands.

Distribution right Brain Innovation possesses international distribution rights for the Phantom exclusively. This right is extended to BI's reseller network based on sales agreements.

Applicable law The Phantom is developed and manufactured at Brain Innovation in Maastricht, The Netherlands. Brain Innovation's jurisdiction is Maastricht, NL. Brain Innovation is also first Seller of the device. In the case there are more Sellers included in the distribution process refer to their sales agreements. Certain rules might be different in other countries.

Warranty of merchantability Brain Innovation warrants that the phantom supplied under this contract shall at the date of delivery:

- be free from defects in material;
- be free from defects in workmanship;
- be free from defects inherent in design, including but not limited to the selection of material, and be fit for the purpose described in section 1.

If any defect provably present in any of the items on the date of delivery comes to light during the defects liability period, then the Buyer shall forthwith notify Brain Innovation or the Seller. Brain Innovation without undue delay, shall at his own risk and cost make good the defect.

Brain Innovation's liability for defects is subject to the Buyer having adherent to all procedures and instructions applicable to the "Conditions of Use" of the Phantom, and expressly excludes damage to the goods caused by fair wear and tear or by misuse occurring after delivery.

Known issues of no defect quality

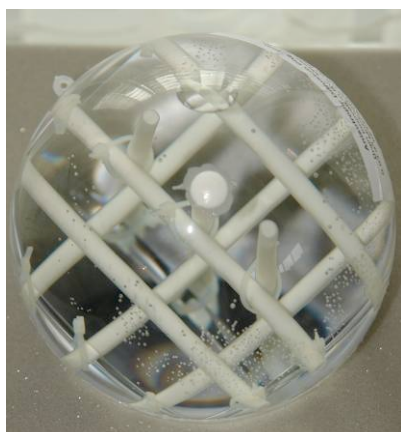


Figure 13: Air bubbles in a straight Anisotropic Phantom model.

There might be some small air bubbles in the phantom. This is unavoidable in the production process, but they will in time aggregate to one air bubble.

If the air bubble has become too large, you might want to add a little demineralized (distilled) water by sticking a needle in the filler cap. A small drop of hard-plastic glue will seal the puncture hole.

There might be small particles floating around in the water. Up to now it is not known that they influence the diffusion in the tubes. Because of their relative big size those molecules are not expected to change the diffusion in the tubes between the synthetic fibers.

When analyzing the data from a scan obtained when the phantom is positioned along the x, y and z direction in the scanner, ADC and FA values may not be equal in the x, y and z oriented phantom tubes. This is an expected result not related to Phantom construction and is probably related to gradient miscalibration [4] and this effect was also observed in human white matter oriented parallel or perpendicular to the main magnetic field [5].

The **defects liability period** shall end twenty-four month after date of invoice or after date of delivery, whichever is later, but in any case not later than twenty five month. The defects liability period shall be extended by a period equal to the period during which the goods cannot be used by reason of any defect, but not so as to extend the defects liability period for more than thirty-six month from the date of first delivery of goods repaired or replaced under this provision.

Notification of defects The Buyer shall notify Brain Innovation or the Seller forthwith of the coming to light of any defect.

The Phantom has been checked by the Manufacturer and Seller before sending. However, it is the Buyer's duty having a first visual inspection of the Phantom after transport.

Furthermore a MR-DTI measurement and comparison with the included product data is suggested to check for more detailed defects caused by transport and handling.

The Buyer needs to send a short descriptive inspection report after receiving the Phantom to the Brain Innovation/ Seller (sales@BrainVoyager.com, Fax +31 43 3884271) within 2 weeks.

In the event of a defect coming to light and being notified to the Seller, the Seller shall, at his discretion and without undue delay repair or replace the defective item at its own risk and cost.

In the event of a defect coming to light (e.g. leaky gasket or broken sphere) the item should not be used in the MR environment to avoid consequential damages of other equipment.

Implied warranty of fitness/ warranty for a particular purpose As evaluated and described in reference 1 the anisotropic Phantom is suitable for the in section 1 circumscribed purpose.

The authors indicate expressively to the [limitations of knowledge transfer](#) collected with the anisotropic Phantom to true organic tissue (nerve fiber bundles). That will be subject of further studies.

7 References

- [1] Pim Pullens, Alard Roebroek, and Rainer Goebel (2010). *Ground truth hardware phantoms for validation of diffusion-weighted MRI applications* JMRI 32: 482-488.
- [2] PL Hubbard, GJM Parker (2009). *Validation of Tractography*. In H Johansen-Berg, TEJ Behrens, *Diffusion MRI: From Quantitative Measurement to In vivo Neuroanatomy*. Elsevier.
- [3] H Johansen-Berg, TEJ Behrens (2009). *Diffusion MRI: From Quantitative Measurement to In vivo Neuroanatomy*. Elsevier.
- [4] Nagy, Z, Weiskopf, N, Alexander, D, and Deichmann, R. (2007). *A method for improving the performance of gradient systems for diffusion-weighted MRI*. MRM 58:763-768.
- [5] J Lee, K Shmueli, M Fukunaga, P van Gelderen, H Merkle, AC Silva, JH Duyn (2010). *Sensitivity of MRI Resonance Frequency to the Orientation of Brain Tissue Microstructure*, PNAS, 107(11):5130-5

Appendix A: Diffusion MRI Concepts

The following section shall explain some theoretical concepts of DTI research for non-experts reading this document. For detailed descriptions we refer to the in chapter 7 scientific literature.

A.1 Diffusion, Isotropic and Anisotropic Diffusion, Diffusion MRI

Diffusion is a mass transport process arising in nature, which results in molecular or particle mixing without bulk motion.

The sensitivity of the **diffusion coefficient** on the local microstructure enables its use as probe of physical properties of biological tissue. On a molecular level diffusive mixing is solely a result of collisions between atoms or molecules in the liquid or gas state.

The physical law that explains this phenomenon is called **Fick's first Law** (Fick 1855 a, b), which relates the diffusive flux to any concentration difference through the relationship

$$J = -D \nabla C$$

J is the net particle flux (vector), C is the particle concentration, and the constant proportionality. In the case of diffusion, the rate of the flux is proportional to the concentration gradient as well as the diffusion coefficient. The diffusion coefficient is an intrinsic property of the medium, and its value is determined by the size of the molecules and the temperature and micro-structural features of the environment.

Isotropic diffusion is a phenomenon explained within Robert Brown's framework of perpetual, random moving particles or here molecules (1828, Brownian motion).

$$\langle x^2 \rangle = 2DT_d$$

Brownian motion is by the Mean square distance *equals 2 times* diffusion constant *times* temperature. E.g. for water at 37°C, $D = 3 \times 10^{-3} \text{ mm}^2/\text{s}$, which is an average displacement of 17µm in 50ms, D is material dependent!

Albert Einstein (1905, 1926) unaware of the other two researchers' work developed a probabilistic framework to describe motion of an ensemble of particles undergoing diffusion, which led to a coherent description of diffusion, reconciling the other two's pictures. He introduced the **displacement distribution** for this purpose, which quantifies the fraction of particles that will traverse a certain distance within a particular timeframe, or equivalently, the likelihood that a single given particle will undergo that displacement.

In free diffusion the displacement is a Gaussian function. Larger diffusion coefficients lead to broader displacement probabilities suggesting increased diffusional mobility. Based on this displacement distribution concept Einstein was able to derive an explicit relationship between the mean-squared displacement of the ensemble, characterizing its Brownian motion, and the classical diffusion coefficient, D , as in Fick's First Law, given by

$$\langle x^2 \rangle = 2D\Delta,$$

where $\langle x^2 \rangle$ is the mean squared displacement of particles during a diffusion time Δ , and D is the same classical diffusion coefficient appearing in Fick's first law.

Following Assaf and Cohen [3], **Diffusion MRI** has the potential to infer features of complex tissue structures as it actually measures the mean displacement of water molecules rather than their diffusion coefficient. Thus, assuming that the displacement of water molecules is affected by tissue microstructure, diffusion MRI should become sensitive to structural parameters of the tissue. ... Biological cells may hinder the Brownian motion (free motion) of extra-cellular water molecules. Inside each cell, diffusion may be envisioned to be restricted by the cellular membranes. Non-free motion may be anisotropic.

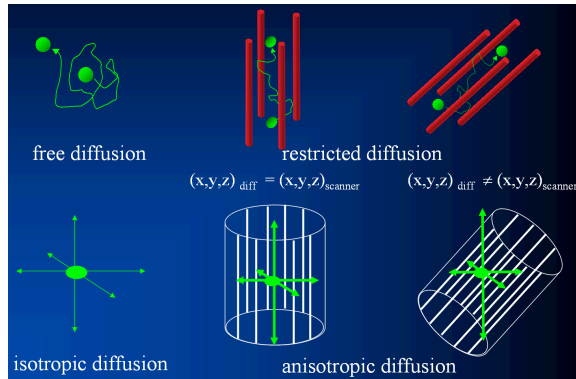


Figure 14: Diffusion types.

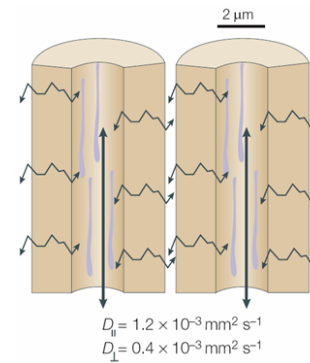


Figure 15: Diffusion directions in neural fibers.

Water is more restricted in its diffusion perpendicular to the axons, than it is parallel to the axons. I.e. Diffusion becomes **anisotropic**: it is larger along some directions than others. $D_{\parallel} > D_{\perp}$

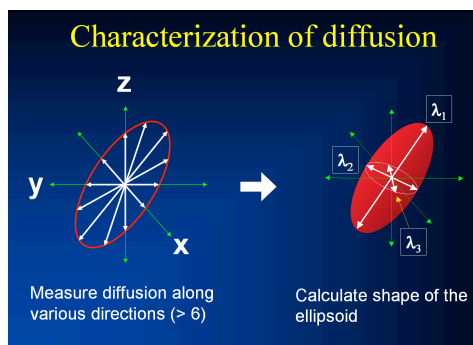


Figure 16: Three magnitudes, three directions.

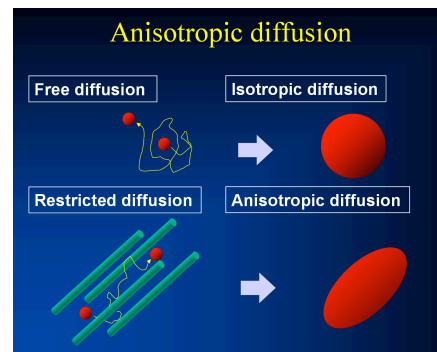
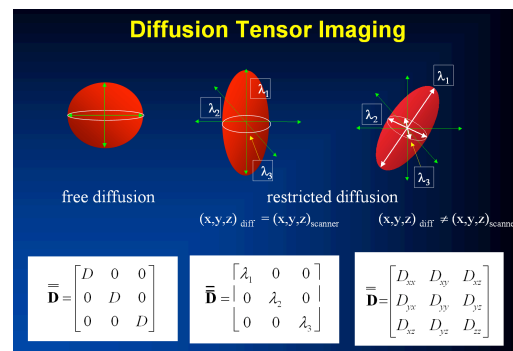


Figure 17: From diffusion to the tensor model.

Isotropic diffusion is free diffusion of molecules with same likelihood to move in all directions resulting in a modeled round diffusion sphere.

Anisotropic diffusion is represented as a diffusion ellipsoid reflecting diffusion parallel or perpendicular to certain structures, in biological tissue/ neural fibers – extra-cellular as well intra-cellular, mainly in the axons.

There is observed evidence that restricted diffusion is apparent in neuronal tissues

with water molecule diffusion within the axons as the main contributor to it (80%) versus 20% extra-cellular. The **intracellular diffusion** is the principle source. Thus, restricted diffusion as measured by MRI enables quantitative, morphologically related, parameters such as the axon density and axon diameter distribution to be extracted.

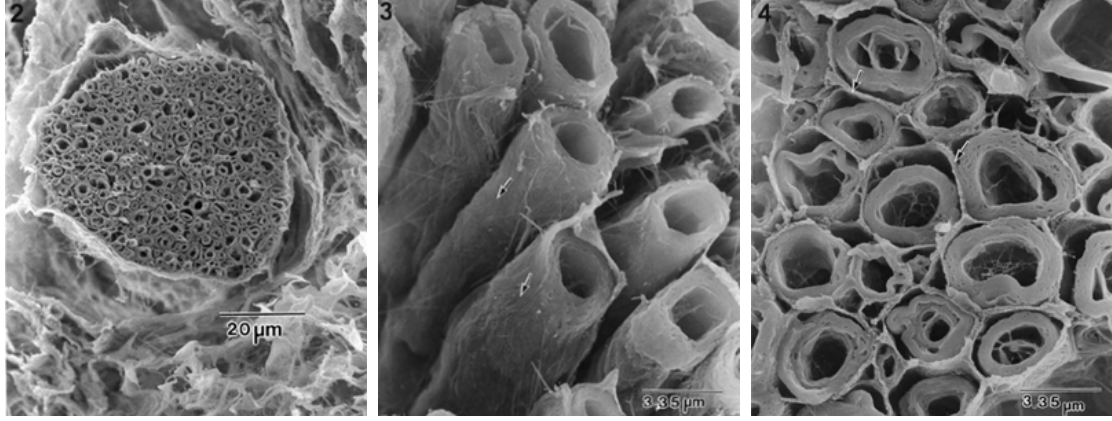


Figure 18: Cell probes of nerve/ axonal bundles.

Different analysis routines and their bio-physical meaning along with selected applications can be tested with the physical synthetic phantom in its defined structural parameters described in section 2.1.

Measured/ apparent diffusion constant. The measured diffusion constant is the **apparent diffusion constant**, not *real diffusion constant*. It is the *statistical average* of all the microscopic displacement distributions which are present in a displayed voxel (spatial unit). It is dependent on the measurement sequence. To probe the direction in tissue we apply gradients in several directions.

The following slides offer a quick discourse through the mathematics:

$$\begin{array}{c}
 \mathbf{S} \quad \mathbf{B} \quad \mathbf{D} \\
 \begin{bmatrix} \ln S_1 \\ \ln S_2 \\ \ln S_3 \\ \ln S_4 \\ \ln S_5 \\ \ln S_6 \\ \ln S_7 \end{bmatrix} = \begin{bmatrix} -b_{xx}^1 & -2b_{xy}^1 & -2b_{xz}^1 & -b_{yy}^1 & -2b_{yz}^1 & -b_{zz}^1 & 1 \\ -b_{xx}^2 & -2b_{xy}^2 & -2b_{xz}^2 & -b_{yy}^2 & -2b_{yz}^2 & -b_{zz}^2 & 1 \\ -b_{xx}^3 & -2b_{xy}^3 & -2b_{xz}^3 & -b_{yy}^3 & -2b_{yz}^3 & -b_{zz}^3 & 1 \\ -b_{xx}^4 & -2b_{xy}^4 & -2b_{xz}^4 & -b_{yy}^4 & -2b_{yz}^4 & -b_{zz}^4 & 1 \\ -b_{xx}^5 & -2b_{xy}^5 & -2b_{xz}^5 & -b_{yy}^5 & -2b_{yz}^5 & -b_{zz}^5 & 1 \\ -b_{xx}^6 & -2b_{xy}^6 & -2b_{xz}^6 & -b_{yy}^6 & -2b_{yz}^6 & -b_{zz}^6 & 1 \\ -b_{xx}^7 & -2b_{xy}^7 & -2b_{xz}^7 & -b_{yy}^7 & -2b_{yz}^7 & -b_{zz}^7 & 1 \end{bmatrix} \begin{bmatrix} D_{xx} \\ D_{xy} \\ D_{xz} \\ D_{yy} \\ D_{yz} \\ D_{zz} \\ \ln S_0 \end{bmatrix} \\
 \mathbf{S} = \mathbf{B}\mathbf{D} \rightarrow \mathbf{D} = \mathbf{S}\mathbf{B}^{-1}
 \end{array}$$

Figure 19: We need at least to measure 6 directions to fill the tensor.

$$\begin{aligned}
 \mathbf{\bar{D}} &= \begin{pmatrix} D_{xx} & D_{xy} & D_{xz} \\ D_{yx} & D_{yy} & D_{yz} \\ D_{zx} & D_{zy} & D_{zz} \end{pmatrix} \xrightarrow{\text{diagonalization}} \vec{v}_1, \vec{v}_2, \vec{v}_3, \lambda_1, \lambda_2, \lambda_3 \\
 ADC &= \frac{\text{trace}(\mathbf{D})}{3} = \frac{(D_{xx} + D_{yy} + D_{zz})}{3} = \frac{(\lambda_1 + \lambda_2 + \lambda_3)}{3} \\
 FA &= \frac{\sqrt{\frac{1}{2} \left[(\lambda_1 - \lambda_2)^2 + (\lambda_2 - \lambda_3)^2 + (\lambda_3 - \lambda_1)^2 \right]}}{\sqrt{(\lambda_1^2 + \lambda_2^2 + \lambda_3^2)}} \quad \begin{array}{l} FA \text{ fully isotropic} = 0 \\ FA \text{ fully anisotropic} = 1 \end{array}
 \end{aligned}$$

Figure 20: From tensor to scalar measures.

A.2 Studying Fiber Configurations and Tractography

Seunarine and Alexander are giving a theoretical overview of this topic in “Multiple Fibers: Beyond the Diffusion Tensor”, see [3].

One central goal when we analyze DTI data is to discriminate between discrete and continuous fibers in special fiber configurations for fiber tracking, like parallel fibers, fanning, bending, acute crossing and general crossing configurations.

Unfortunately, DTI acquisitions produce only a discrete, coarsely sampled representation $[v(l, j, k)]$ of the continuous fiber tract direction field $[v(x, y, z)]$. That makes certain configurations extremely difficult to classify (e.g. crossing versus touching). Our goal is to reconstruct trajectories of bundles of fibers from the direction field extracted from diffusion tensor data in the phantom configuration. This can be done within BrainVoyager QX or with other software algorithms.

The discrimination of such problematic properties even in a synthetic phantom are dependent on the DTI acquisition sequence, magnetic field properties (e.g. homogeneity) and other acquisition parameters, voxel resolution, position of the phantom relative to the magnetic field, post-hoc data correction algorithms, reconstruction algorithms beside other variables adding in in-vivo measurements of human brain structure (e.g. head motion etc.).

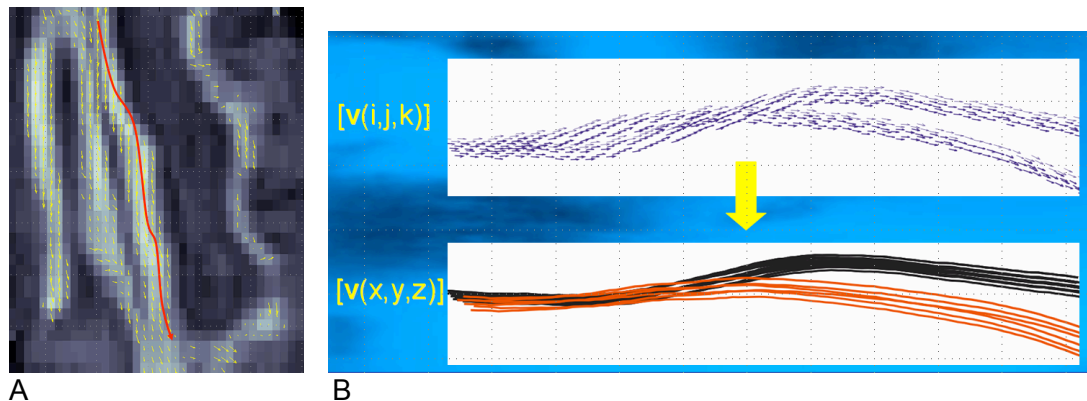


Figure 21 A: Voxel-based DTI data in volume-space with tensors; B: Discrete, coarsely sampled representation $[v(l, j, k)]$ of the continuous fiber tract direction field $[v(x, y, z)]$ and reconstruction of trajectory fiber bundles.